Title	Geometrical analysis of the refraction and segmentation of normal faults in periodically layered sequences
Author(s)	Schöpfer, Martin P. J.; Childs, Conrad; Walsh, John J.; Manzocchi, Tom; Koyi, Hemin A.
Publication Date	2007-02
Publication information	Journal of Structural Geology, 29 (2): 318-335
Publisher	Elsevier
Link to publisher's version	http://dx.doi.org/10.1016/j.jsg.2006.08.006
This item's record/more information	http://hdl.handle.net/10197/3032
Rights	This is the author’s version of a work that was accepted for publication in Journal of Structural Geology. Changes resulting from the publishing process, such as peer review, editing, corrections, structural formatting, and other quality control mechanisms may not be reflected in this document. Changes may have been made to this work since it was submitted for publication. A definitive version was subsequently published in Journal of Structural Geology Volume 29, Issue 2, February 2007, Pages 318-335 DOI#: 10.1016/j.jsg.2006.08.006 .
DOI	http://dx.doi.org/10.1016/j.jsg.2006.08.006

Geometrical analysis of the refraction and segmentation of normal faults in periodically layered sequences

Martin P.J. Schöpfer [a,*], Conrad Childs [a], John J. Walsh [a], Tom Manzocchi [a], Hemin A. Koyi [b]

[a]*Fault Analysis Group, School of Geological Sciences, University College Dublin, Belfield, Dublin 4, Ireland*

[b]*Department of Earth Sciences, Uppsala University, Villavägen 16, SE-752 36 Uppsala, Sweden*

Abstract

Normal faults contained in multilayers are often characterised by dip refraction which is generally attributed to differences in the mechanical properties of the layers, sometimes leading to different modes of fracture. Because existing theoretical and numerical schemes are not yet capable of predicting the 3D geometries of normal faults through inclined multilayer sequences, a simple geometric model is developed which predicts that such faults should show either strike refraction or fault segmentation or both. From a purely geometrical point of view a continuous refracting normal fault will exhibit strike (i.e. map view) refraction in different lithologies if the intersection lineation of fault and bedding is inclined. An alternative outcome of dip refraction in inclined multilayers is the formation of segmented faults exhibiting en échelon geometry. The degree of fault segmentation should increase with increasing dip of bedding, and a higher degree of segmentation is expected in less abundant lithologies. Strike changes and associated fault segmentation predicted by our

* Corresponding author.
Email: martin@fag.ucd.ie

geometrical model are tested using experimental analogue modelling. The modelling reveals that normal faults refracting from pure dip-slip predefined faults into an overlying (sand) cover will, as predicted, exhibit systematically stepping segments if the base of the cover is inclined.

Keywords: Fault geometry; fault refraction; fault segmentation; en échelon; sandbox modelling;

1 Introduction

Normal faults contained in multilayer sequences show a range of geometrical complexities arising from propagation-related phenomena (Fig. 1). For example, fault traces observed in cross-section are often refracted with steeply dipping segments in the strong layers and shallow dipping segments in the weak ones (Wallace, 1861; Dunham, 1948; Ramsay and Huber, 1987; Dunham, 1988; Peacock and Zhang, 1993; Mandl, 2000; Sibson, 2000; Ferrill and Morris, 2003; Fig. 1b). Fault refraction, referred to as ‘steep and flat structure’ in Ramsay and Huber (1987, p.518), has been variously attributed to either different modes of fracturing (e.g. Ferrill and Morris, 2003) or to different friction coefficients within the interbedded lithologies (e.g. Mandl, 2000). A difference in mode of fracture within individual layers typically occurs at low effective stress, where one lithology (the ‘strong’ one) has a strength that facilitates failure in tension, whereas the other lithology (the ‘weak’ one) fails in shear (Schöpfer et al., 2006). Another propagation-related characteristic of normal faults is that they often display segmentation in 3D (Ramsay and Huber, 1987; Peacock and Sanderson, 1994; Childs et al., 1995; Childs et al., 1996; Walsh et al., 1999; Walsh et al., 2003), providing fault segment traces that step laterally in plan view (Segall and Pollard, 1980; Peacock and Sanderson, 1991; Peacock and Sanderson, 1994; Childs et al., 1995). If the stepping of fault segments or fractures is systematic, the resulting geometry is commonly referred to as en échelon. Stepping faults can either overlap or underlap and the distance between the tips of the two faults measured parallel to the segments is the overlap (or underlap) length. Increased displacement on overlapping segments leads to the steepening of intervening relay ramps and eventually to the formation of fault-bound lenses (e.g. Larsen, 1988; Peacock and Sanderson, 1991; Walsh et al., 1999; Imber et al., 2004; Fig. 1c). Despite the importance of fault refraction and segmentation in the growth of fault zones, very few mechanical/numerical models incorporate both processes (Mandl, 2000).

When a fault surface propagates through a rock volume it rarely does so as a single continuous surface but as an irregular and, to a greater or lesser extent, segmented array. Segmentation is due to local retardation or acceleration of propagation of the fault tip-line controlled by the heterogeneous nature of the rock volume (e.g. Jackson, 1987): heterogeneities occur on a range of scales, from grain-scale to crustal scale. A fundamental question regarding the propagation of faults is, under which states of stress or strain is a fault expected to be (systematically) segmented? One way of addressing this question was proposed by Mandl (1987; revisited by Treagus and Lisle, 1997) who showed that Coulomb-Mohr shear failure planes will be discontinuous within homogeneous, isotropic volumes if continuous $\sigma_{I}\sigma_{II}$-principal planes of stress cannot be defined. Mandl's method (1987), however, has not yet been developed into a scheme for predicting the detailed 3D geometry of segmentation within a multilayer sequence. Another approach is to investigate the 3D state of stress or strain in two different materials that are separated by a coherent interface (Treagus, 1981; Goguel, 1982; Treagus, 1983 and 1988; Mandl, 2000). These studies have shown, that under many circumstances (e.g. when none of the principal axes of stress or strain are contained within an interface, or when a shear couple is applied to two layers with different initial differential stress) principal planes of stress or strain will be discontinuous across the interface. As Treagus (1988) points out, it is, however, difficult to justify the application of this approach to faulting within multilayers, because it requires the unlikely scenario that the onset of faulting occurs simultaneously in the two materials (Treagus, 1988; Mandl, 2000).

In this paper we use an alternative approach, which is non-mechanical and purely based on geometry, to investigate the circumstances in which faults are expected to be segmented within dipping multilayer sequences. Our simple geometric model of normal faults suggests that fault segmentation and/or map view (i.e. strike) refraction are inevitable consequences of fault dip refraction within dipping multilayer sequences. The basic characteristics of this model are illustrated using a simple stereonet construction showing that a continuous normal fault that refracts across a inclined bedding plane will also refract in map view if the strike of bedding and the fault are not the same (Fig. 2). In these circumstances strike refraction arises because the fault/bedding intersection lines are different for different layers (Fig. 2a); this does not occur when the fault and bedding have the same strike. Although coeval dip and strike refraction provides a means of generating a continuous fault, it requires different amounts of oblique-slip motion over different parts of the continuous fault surface (Fig. 2b and 3b). An alternative outcome, which does not require oblique-slip motion, is that the geometrical complications arising from differing fault/bedding intersection lines for different layers are accommodated by the localisation of segmented dip-slip fault arrays (Fig.3c), where the degree of segmentation depends on the relative geometries of fault and bedding: for the purposes of this paper, the degree of segmentation is the number of segments per unit length along a segmented fault array. This geometrical model provides a means of estimating the geometry and degree of fault segmentation, an approach which is tested using a plane strain physical model of faulting within a cover sequence above an underlying predefined fault with a inclined intersection with the base-cover interface. The experimental modelling results verify our geometrical approach and demonstrate, for example, that systematic stepping of fault segments in the cover above a reactivated basement fault are not necessarily kinematic indicators for oblique-slip reactivation. We then show how our simple model offers one plausible mechanism for generating highly segmented fault arrays including that shown in Fig. 1. We suggest that a continuous (non-segmented) fault in a multilayer may be the exception rather than the rule and that lithological/mechanical stratigraphy is extremely important for understanding the segmented nature of faults. This study focuses on normal fault geometries within gently dipping beds for two reasons: (i) The geometry of normal faults within horizontal to gently dipping layering is better defined than for normal faults within steeply dipping beds. (ii) Dramatic fault dip variation (refraction) often requires that layers fail in different modes (extension vs. shear failure), which is promoted at low effective stress and therefore more likely in extensional settings (e.g. Sibson, 1998). Nevertheless, our approach and general findings could be applicable to any type of fault showing fault refraction within multilayer sequences.

2 Introduction to geometrical analysis

The aim of this paper is to describe methods for evaluating the likely impact of differences in fault dip in different lithologies on fault surface geometry. The purely geometrical approach adopted in this study requires only a few known parameters, which can be quite often estimated for natural systems. The parameters include (i) the dips of normal faults in the two different lithologies comprising the periodically layered sequence, (ii) the thickness ratio of the two lithologies and (iii) the orientation of bedding relative to the average fault plane (which is taken to be the enveloping surface of a refracting fault). Figure 3 introduces the geometries that will be discussed in detail in the following two sections, Fig. 2 illustrates some of the geometrical parameters discussed and a list of symbols is given in Table 1. Figure 3a shows a block diagram and the stereonet solution for a planar (i.e. non-refracting) normal fault in a dipping sequence. Figure 3b shows the same sequence with a normal fault exhibiting refraction. The refracted nature of the fault plane when combined with bedding which has a different dip direction leads to a situation in which fault-bedding intersections within each lithology are different, with neither being parallel to the intersection of bedding and the ‘average’ fault plane through the multilayer (Fig. 2a). This geometric problem could be solved by generating a continuous fault plane, but this requires different fault dip directions and differing departures from pure dip-slip motion in the two lithologies (Figs. 2b and 3b). In Section 3 we consider some of the geometrical implications of this continuous fault model, which is one end-member geometry considered in this study. Figure 3c shows another quite different solution to the geometrical problem, with the fault localising first in the strong layers as an array of en échelon segments, each of which is dip-slip and has the same dip direction as the ‘average’ fault. This model does not involve geometries that demand strike changes and associated oblique-slip motion, but does require fault segmentation which is in fact a relatively common phenomenon associated with faults. This model, which is our favoured solution to the geometrical issues confronted by fault growth through dipping multilayers, is the other end-member geometry considered in this study, and is described in more detail in Section 4.

3 Continuous refracting faults

3.1 *Geometry*

For the geometrical model of a continuous refracting fault (Fig. 3b) we make the following assumptions: (i) Fault dips in the individual lithologies comprising the multilayer are constant irrespective of their strike or the orientation of layering. (ii)

The multilayer sequence is periodically layered and consists of two materials that exhibit different fault dips. (iii) Layers containing steep and shallow dipping faults are taken to be "strong" and "weak" respectively, an assumption which is true in many if not all circumstances. The block diagram shown in Fig. 3b illustrates the 3D geometry of a continuous refracting fault. The fault trace refracts both in cross-section and in map view. The geometry of this fault can be obtained using a stereonet or numerically.

3.2 *Stereonet solution*

Consider a refracting normal fault in a periodically layered sequence consisting of two different materials. The fault dip in the strong and weak material is θ_s and θ_w, respectively, and the average fault dip, θ_a, is somewhere in-between. Bedding is not necessarily horizontal and need not have the same dip direction as the fault. The thickness ratio, t_s/t_w, of the two materials, which is the thickness of the strong layers divided by the thickness of the weak layers in the periodically layered sequence, is a variable which can either be prescribed or derived (see below). A simple stereonet construction (Fig. 4a) reveals that when the bedding dip direction is oblique to the fault dip direction, formation of a continuous refracting fault surface, which refracts at the bedding plane, is complicated by the fact that the fault planes in the two materials do not share the same intersection lineation with the bedding plane. In order to obtain a continuous surface the dip direction in one of the two materials could be changed (Figs. 4b and c). However, this leads to a change of the average dip direction. A continuous refracting fault therefore demands a change of dip direction of the faults contained in both materials (Fig. 4d). The intersection lineation of the fault planes in the two materials with the bedding plane is the same and contained within the average fault plane. The intersection lineation of the average fault with the bedding plane is the pole to a great circle that, in the case of a continuous fault, contains the poles of the faults in the strong and weak layers. This great circle could be called the fault *π*-circle, in accordance with the nomenclature used for cylindrical folds. In the example shown in Fig. 4d the fault in the strong layers (f_s) is rotated clockwise relative to the average fault (f_a) whereas the fault in the weak layers (f_w) is rotated anti-clockwise. The average fault dip (θ_a) is a function of (i) the fault dips in the strong and weak layers, (ii) the orientation of bedding (subscript *b*) relative to the orientation of the average fault, and (iii) the thickness ratio of the two materials t_s/t_w. Measured in a vertical section perpendicular to the strike of the average fault the following relationship, which is derived in Appendix A, is obtained:

$$\frac{t_s}{t_w} = \left[\frac{\tan(\theta_a - \theta'_b)}{\tan(\theta'_w - \theta'_b)} - 1\right]\left[1 - \frac{\tan(\theta_a - \theta'_b)}{\tan(\theta'_s - \theta'_b)}\right]^{-1} \tag{1}$$

where the apparent dips (primed values) are measured in this section. Thus, for predefined fault dips in the strong and weak layers and a predefined dip of the average fault, one can obtain the thickness ratio using the stereonet and Eq. (1). Alternatively, the same geometric problem can be solved numerically for predefined fault dips in the strong and weak layers and for a predefined thickness ratio.

3.3 *Numerical solution, maps and cross sections*

In the following analysis[1] the constants are: (i) the fault dips in the strong and weak layers, θ_s and θ_w, respectively, (ii) the average fault dip direction, ϕ_a, and (iii) the thickness ratio, t_s/t_w. The orientation of bedding, ϕ_b and θ_b, is varied systematically and the dip directions of the fault in the strong and weak layers, ϕ_s and ϕ_w, respectively, and the average fault dip, θ_a, are obtained from Eq. (1) by converging to the solution using the bisection method. In order to illustrate the geometries clearly we chose a thickness ratio of 1.0 and fault dips in the strong and weak layers of 80° and 50°, respectively. These dip values and a fault refraction of 30° are typical for normal faults in limestone/mudrock sequences where faulting occurred under low effective stress (Peacock and Zhang, 1993; fig. 4). A sensitivity study where we varied the thickness ratio and the fault dips in the strong and weak layers is given later in this section.

Contour plots of strike refraction, i.e. the change in strike from one lithology to the other, and the average fault dip as a function of bedding orientation relative to the orientation of the average fault are shown in Fig. 5. These plots reveal that, if bedding is dipping and has a different strike to the average fault, strike refraction occurs and the amount of refraction increases with increasing dip of bedding (Fig. 5a). Figure 5b shows that the average fault dip is a function of bedding orientation, though for the particular geometrical parameters chosen it only varies by about 10º. Additionally Fig. 5b reveals that for a particular dip of bedding the average fault dip attains its maximum value when bedding dips in the opposite direction to that of the average fault. Maps constructed using the strike-change data obtained from this

---

[1] A MATLAB® script for obtaining the geometry of a continuous refracting fault in a periodically layered sequence is provided as an electronic supplement.

approach are shown in Fig. 6a. These maps illustrate the zigzag geometry of the fault trace (strike refraction) and also show that the amount of strike refraction increases with increasing dip of bedding (Fig. 5a). The cross sections (Fig. 6b) illustrate that the average fault dip increases as the difference in dip direction between the average fault and bedding increases (Fig. 5b).

As stated above, we selected a thickness ratio of 1.0 and fault dips in the strong and weak layers of 80° and 50°, respectively, to illustrate the range of continuous fault geometries that are obtained when the orientation of bedding is varied. The dependencies obtained (Figs. 5 and 6) also hold for different values of θ_s, θ_w and t_s/t_w, though the geometrical details will vary as a function of these three parameters. We therefore investigated the impact of thickness ratio and dip refraction on fault geometry. Figure 7a shows three map view examples of continuous refracting faults in periodically layered sequences with thickness ratios of 0.1, 1.0 and 10. The graphs in Fig. 7b and c show the differences in dip direction between the fault contained in the strong and weak layers and the average fault as a function of thickness ratio. In Fig. 7b the fault dips in the strong and weak layers are 80° and 50°, respectively, and the dip of bedding is 30º. Curves are plotted for five different orientations of bedding; we therefore vary the thickness ratio for the maps shown in the third row in Fig. 6a. We also investigated the effect of fault dips in the strong and weak layers (fault dip refraction) and thickness ratio on strike refraction (Fig. 7c) for a dip of bedding of 30º and strike difference between average fault and bedding of 90º; we therefore vary both the thickness ratio and the fault dip refraction for the central map in the third row in Fig. 6a. The strike refraction in these graphs is the distance between corresponding labelled curves and varies slightly as a function of thickness ratio. The change in fault strike in the different lithologies ($\phi_s - \phi_a$ and $\phi_w - \phi_a$), however, strongly depends on the thickness ratio (Fig. 7). The maps and curves reveal that fault strike changes are typically greater in the less abundant material (see Fig. 7a). Additionally Fig. 7c reveals that the greater the dip refraction the greater the associated strike refraction.

Although this section highlights some interesting geometrical properties of continuous refracting faults, it is not yet clear whether these types of geometries often occur in nature. As a consequence we have extended the results obtained in this section to consider a more likely geometrical model in which segmented arrays of faults, rather than continuous refracting faults, arise from the associated complications of differing fault and bed orientations (Fig. 3c).

4 Discontinuous refracting faults

4.1 *Geometry*

The zigzag fault geometry predicted by the continuous fault model (Fig. 6a) implies that the fault has oblique-slip components, which are in opposite senses in the strong and weak layers. Field evidence and numerical modelling of small-scale normal faults in high strength contrast multilayer sequences suggest that normal faults first localise within the strong/brittle layers as steeply dipping dip-slip faults or extension fractures which are later linked via shallow dipping faults in the weak/ductile layers (Peacock and Zhang, 1993; Crider and Peacock, 2004; Schöpfer et al., 2006). Thus a more realistic and our favoured initial geometry is that the fault localises in the strong layers as dip-slip faults with dip directions parallel to the average fault, which, in dipping layers, is only possible if it forms an en échelon array. In these circumstances the 3D geometry of segmented refracting faults can be derived relatively simply from, and related to, those of the continuous faults shown in Fig. 3b and described in the previous section. Assuming that the fault in the strong layers localises as an en échelon array of dip-slip faults and that these segments have the same dip direction as the average fault, then the median plane through the en échelon array will have the same orientation as the continuous fault in Fig. 3b. A block diagram showing a fault array geometry that satisfies these requirements is shown in Fig. 3c. In the following we use our simple geometric model to quantify the degree of segmentation in map view as a function of bedding orientation. A prerequisite of this exercise is, however, to define geometrical parameters that describe the geometry of en échelon arrays.

4.2 *Overlap length and fault separation*

The geometry of fault arrays with en échelon geometry can be described using the following parameters, all of which are measured in a horizontal plane in this study: (i) fault segment length, L, (ii) overlap length, O, which is the length of the rectangular region that is bounded by two neighbouring segments, (iii) separation, S, which is the normal distance between two neighbouring segments, and (iv) the difference in strike between the individual fault segments and the average fault array, ψ (Fig. 8a). These four parameters are related by the simple relationship

$$S = (L - O)\tan\psi \tag{2}$$

Although the geometry of an en échelon array can therefore be fully described by three parameters, the number of parameters can be reduced to two by introducing the overlap length to separation ratio, O/S, which is 2 – 4 for natural and experimental normal fault arrays (Soliva and Benedicto, 2004; Hus et al., 2005). The en échelon arrays shown in Fig. 8 were drawn using Eq. (2) for constant segment lengths L (Fig.

8b) and for constant separations S (Fig. 8c), for different values of ψ and O/S. From these maps one can conclude that as the inclination of the segments, ψ, increases the degree of segmentation increases, regardless of whether we keep the segment length or the separation constant.

4.3 *Maps of discontinuous faults*

As stated above we assume that the fault segments within the strong layers have the same dip direction as the average fault since they nucleate as dip-slip faults. The strike differences between the average fault and the faults in the strong and weak layers, $\phi_s - \phi_a$ and $\phi_w - \phi_a$, respectively, that were obtained for continuous faults can then be used to construct maps of discontinuous faults using Eq. (2) (see Fig. 8). This requires that we keep the overlap to separation ratio and the length of one parameter in Eq. (2) constant. For direct comparison with the continuous fault results, we have chosen a thickness ratio of 1.0. Median planes through the en échelon arrays within the strong layers have a dip of 80° and the (unsegmented) faults within the weak layers have a dip of 50°. Figure 9a shows maps constructed using the data obtained from the analysis of continuous faults and using Eq. (2) with a constant separation and an overlap to separation ratio of three (Fig. 8c); note that these maps are not horizontal slices (as shown in Fig. 6a), but are top views of the bedding plane. Essentially, these maps are aerial views of the top of a strong layer within a multilayer, where the overlying layers have been eroded. Consequently cut-effects arise in these maps, e.g. the segment traces are not oriented N-S, despite the fact that their dip direction is 270º. A line joining the centres of the fault segments in these maps is the intersection lineation of bedding with (i) the median plane through the en échelon segments, (ii) the fault in the weak layers and (iii) the average fault plane (Fig. 3c).

The maps show that degree of segmentation generally increases with increasing dip of bedding (Fig. 9a). The basic results for discontinuous faults are similar to the results presented above for continuous faults, because the difference in dip direction for the continuous fault (median plane through en échelon array) is the ψ- value in Eq. (2), which determines, for a given overlap to separation ratio, the degree of segmentation (Fig. 8). Thus the sensitivity study of geometrical parameters presented above for a continuous fault (Fig. 7) can be used to predict the degree of segmentation. Therefore, for example, we can infer that refracting faults within dipping multilayers are expected to exhibit a higher degree of segmentation in the less abundant lithologies. Cross sections of segmented fault shown in Fig. 9b were constructed by randomly selecting sections along the maps shown in Fig. 9a and by using the same bedding geometries as shown for continuous faults in Fig. 6b. We did not introduce another parameter that takes into account the separation of the segments as a function of bed thickness since under many circumstances no clear relationship between fracture spacing and bed thickness exists (e.g. Olson, 2004). Despite these limitations the cross sections shown in Fig. 9b illustrate that the frequency of occurrence of two segments within a strong layer generally increases with increasing dip of bedding.

In this section we only determined the possible degree of fault segmentation within the strong layers. Maps and cross sections similar to Fig. 9 can also be determined for the weak layers. The general results obtained for the strong layers also hold for the weak layers, though the stepping direction of the fault segments will be in the opposite direction. This is because the median planes through the en échelon arrays in our discontinuous model are the solutions for the continuous fault model, where the faults in the two different lithologies exhibit strike changes in opposite direction (Figs. 3b and 4d).

5 Experimental modelling of discontinuous faults

5.1 *Methodology and boundary conditions*

The previous two sections considered continuous and discontinuous refracting faults, respectively, which could be considered either as geometrical end-members, or stages within a growth sequence. Many studies of natural faults have shown that faults often grow as initially segmented (discontinuous) arrays that are progressively linked with increasing displacement to form a continuous fault (e.g. Peacock and Sanderson, 1994; Childs et al., 1995, 1996). Although our geometrical analysis cannot predict whether faults in dipping multilayers are likely to be initially segmented or continuous, our preconception, based on outcrop studies of small scale faults, is that segmented faults are the more likely to occur. In this section we therefore present a suite of small-scale physical experiments which was designed to test our simple geometrical model whether or not segmented fault arrays with systematic stepping form under boundary conditions which are broadly equivalent to those of our geometric model.

We used the sandbox modelling technique, a well-established method for modelling the development of faults in isotropic, homogeneous brittle rock (e.g. Mandl, 1988). The analogue material was dry quartz sand with a friction angle, φ, of 33 ± 4°. Normal faults that develop in this analogue material are expected to have a dip of 45° + φ/2, i.e. approximately 61.5 ± 2°, according to the Coulomb-Mohr theory of faulting, and this value is confirmed in the models. A detailed account of the scaling of physical experiments and of the justification and limitations of using dry sand as an analogue material for brittle rock can be found in Mandl (2000; chapter 9).

For the purpose of this study we investigated the propagation of predefined ‘basement ‘ faults into a ‘cover’ sequence. There are a variety of scenarios for which our boundary conditions are appropriate, such as the reactivation of a faulted substrate overlain by an unfaulted sedimentary sequence. Alternatively the model could represent the propagation of a fault across the interface between two layers, from one type of layer, characterised by particular properties and a related fault dip, into an overlying layer, characterised by a different fault dip. For simplicity we will refer to the rigid blocks containing the predefined faults as *base* and the overlying sand as *cover*; the boundary between these two ‘units’ is the *base-cover interface*.

In all of the three experimental configurations used a central wedge shaped base block, the hangingwall block, fits exactly between two footwall blocks (Fig. 10). The two predefined faults have a dip of 45º in all models and the dip of the base-cover interface is 0, 10 and 20º (Fig. 10a, b and c, respectively). The dip directions of the predefined faults and the base-cover interface are perpendicular to each other; the intersection of an inclined base-cover interface (Fig. 10b and c) with the predefined fault is therefore not horizontal, a feature which will be discussed below. The base blocks are confined laterally by glass plates and whilst one of the footwall blocks is fixed, the other is connected to a geared motor. The cover sequence consists of alternating layers of coloured loose sand, each layer of which is prepared by scraping piles of loose sand to the desired thickness. Faulting within the cover sequence is achieved by pulling the moveable footwall block with a velocity of *ca* 10cm/h; as a consequence the hangingwall block slides downwards under its own weight.

Our model configurations enforce fault refraction at the base-cover interface, because the predefined faults have a 45° dip, which is lower than the dip of normal faults that develop within the cover sequence (expected fault dip of 62°). Furthermore, relative to the intersection between the predefined fault and the base-cover interface, the mode of faulting changes with the dip of the base-cover interface. For example, in the case of a horizontal base-cover interface the predefined fault represents a Mode II dislocation, since the slip vector is perpendicular to the fault-interface intersection (Fig. 10a). For a dipping base-cover interface, the predefined fault is a mixed Mode II & III dislocation, since the slip vector is oblique to the fault-interface intersection (Fig. 10b and c). Each model was extended by the same amount of bulk extension (40 mm), with each predefined fault having a final throw of 20 mm at the base-cover interface. The surface of each model was photographed in 2 mm throw. Once completed, each model was saturated with water so that vertical sections could be generated and photographed for subsequent analysis. Since the resulting fault pattern in each model is symmetric we only present the results for one fault zone from each configuration.

5.2 *Stereonet prediction*

As a prelude to presenting our model results, stereonet solutions, based on our geometrical model, can be constructed for the experiments (left column in Fig. 11). For convenience we choose a geographic reference frame where the predefined fault of the fixed footwall block dips towards the south (180/45; Fig. 10). In the case of an inclined base-cover interface the interface dips towards the west (270/10 and 270/20, Fig. 10b and c, respectively). The plunge direction and plunge of the predefined fault / base-cover interface intersections for the three configurations are therefore (270/00), (260/10) and (250/19). In addition we can assume that antithetic faults, which nucleate at these intersections, will develop in the cover sequence due to the change in fault dip (i.e. at the kink of the sliding path as referred to by Mandl, 1988). A continuous refracting fault demands that the intersection of the cover faults be the same; consequently, using a dip of 62°, the dip directions of the syn- and antithetic faults can be constructed and are 180° (no strike change) in case of the horizontal base-cover interface, 175° (synthetic) and 345° (antithetic) for the 10° dipping interface, and 170° (synthetic) and 330° (antithetic) for the 20° dipping interface (Fig. 11). If our geometrical model is valid, we therefore expect the following: (i) Neither strike change nor systematic stepping of faults developing in the cover above the horizontal interface (Fig. 11a). (ii) Either left-stepping dip-slip fault segments or continuous dextral-oblique-slip normal faults within the cover above the inclined interfaces (Fig. 11b and c).

5.3 *Experimental results*

5.3.1 *Horizontal base-cover interface*

The earliest faults, which develop fault traces at the surface of the model, are steep synthetic faults, which are referred to as precursor faults in the literature (e.g. Horsfield, 1977). With increasing displacement, one and sometimes two shallower dipping synthetic faults develop in the footwall. Precursor faults do not extend along the entire length of the predefined fault and subsequently link along strike with shallower dipping synthetic faults to form undulating fault traces in map view (Fig. 11a). Although this type of fault segmentation leads to the formation of short-lived relays, stepping of these fault segments is not systematic. With increasing displacement a single, through-going and straight master fault develops in the footwall of the precursor faults and the fault scarp gradually collapses. The master fault has a dip of *ca* 60º as expected form the friction angle of the sand. Two or three antithetic adjustment faults also develop within the models. New antithetic faults develop in the hangingwall of earlier antithetics, and together with contemporaneous slip along synthetic faults leads to the formation of a secondary graben that deepens and becomes narrower with increasing displacement (see cross section in Fig. 11a).

5.3.2 *Dipping base-cover interface*

Models with a dipping base-cover interface have a wedge-shaped cover sequence, which thins towards the east (Fig. 10b and c). Although faults in the thinner parts of the cover show more advanced stages of fault growth, the fault pattern is similar for a given throw to cover thickness ratio. For a 20º dipping interface initially E-W striking precursor faults exhibit a systematic left-stepping (at predefined fault throws of *ca* 4 mm; Fig. 12). With increasing displacement the western tip of each segment typically propagates towards the west, whereas the eastern tip propagates towards the NE to link with another segment (at throws of *ca* 8 mm; Fig. 12). The linkage leads to hangingwall breaching of individual relays, with hangingwall segments propagating and linking with the footwall segments. Further displacement causes rotation of the breached relays, which only ceases when a through-going synthetic master fault is developed, and the array of precursory structures becomes inactive: because of fault scarp collapse, abandoned splays are not as easily seen where the fault scarp is first developed and where the cover is thinner. The average dip of this complex synthetic master fault zone is *ca* 60º and the dip direction is in perfect agreement with our stereonet prediction, i.e. 170º, a geometry which was originally represented by an array of fault segments (Fig. 12). Two or three antithetic faults develop, which exhibit systematic stepping on the mm-scale, which therefore cannot be seen from the photographs. The dip directions of the antithetic fault zones are in agreement with our stereonet prediction, i.e. 330º. The model with a 10º dipping interface is, as predicted, characterised by a similar fault zone evolution but with a less dramatic change in dip direction relative to the predefined fault and with the development of fewer relays (Fig. 11b). In both models contemporaneous movement along synthetic and antithetic faults leads to the formation of a secondary graben that narrows towards the east, i.e. towards the thinner part of the model.

6 Interpretation of natural example

In previous sections we introduced a simple model for the formation of segmented normal faults arising from fault refraction. We later verified our model using a suite of physical experiments. In light of our model we now re-examine the field example (Fig. 1) of an oblique-sinistral normal fault within a limestone/shale multilayer sequence, Kilve foreshore, Somersest, UK (see Glenn et al., 2005, for geological background of this area). The fault zone exhibits fault dip refraction (Fig. 1b), with an average fault dip difference between the limestone and shale beds in the range of 20º to 30º, and map view segmentation, with right-stepping segments (Fig. 1c). Within the shale layers good kinematic indicators (slickensides) are exposed, whereas within the limestone layers calcite infilled pull-aparts developed, that indicate precursory extension fracturing (Fig. 1a). Orientation data of the fault zone are shown in Fig.13a, together with the mean orientations of bedding, faults within the limestone and shale, and a slickenside lineation within the shale. The orientation data show that there is a strike difference between the faults in the limestone and shale layers and that the slip vector is oblique to fault/bedding intersections. Although this fault zone therefore represents a good field example for testing our model, ready comparison with our model and with associated stereonets (Fig. 4) is made much easier by rotation of the slickenside lineation together with associated orientation data in such a way that (i) the fault in the shale is dip-slip with a dip of 50º and (ii) bedding is dipping towards the south (Fig. 13b). Using the intersection of bedding with the fault within the shale, we constructed a continuous refracting fault with a fault dip within the limestone layers of 80º. The strike difference between the fault within the shale and the constructed continuous fault within the limestone layers is 24º (Fig. 13b). According to our model, therefore, we would expect a high degree of fault segmentation, with right-stepping segments within the limestone layers, and this is exactly what we observe (Fig. 1c). The measured mean dip direction of the fault segments within the limestone (ϕ = 271) is slightly different in comparison to the dip direction predicted for a continuous fault (ϕ = 282; Fig. 13b). We believe that this reflects the fact that the fault is segmented and exhibits systematic stepping, with segments that strike almost sub-perpendicular to the extension direction.

7 Discussion

Fault refraction is a well-documented feature of normal faults contained in multilayer sequences and occurs on a large range of scales (mm – km). Best seen on cross-sectional views of faults, refraction is most often a response to different mechanical properties of different lithologies (fault refraction due to differential compaction after faulting, e.g. Davison, 1987, is not discussed here). By contrast, another propagation-related phenomenon, fault segmentation, is best seen in map view of normal faults and is also a common feature of normal faults at least in their earliest stages of growth. In this paper we have developed a simple geometric model of normal faults suggesting that fault segmentation and/or strike refraction are inevitable consequences of fault dip refraction within dipping multilayer sequences. This geometrical model provides a means of estimating the geometry of 3D fault refraction and/or segmentation within multilayered sequences, an approach which we have tested using a series of plane strain physical modelling of faulting within a cover sequence above an underlying predefined fault. Our simple model suggests that the degree of fault segmentation and/or strike refraction will increase with increasing dip refraction between layers, a feature which will be promoted by high strength contrasts between layers. The model emphasizes that a continuous (non-segmented) fault in a multilayer may be the exception rather than the rule and that lithological/mechanical stratigraphy is an extremely important factor for understanding the segmented nature of faults. The experimental modelling results support our geometrical approach and demonstrate, for example, that systematic stepping of fault segments in the cover above a shallow dipping, predefined fault is not necessarily a kinematic indicator for oblique-slip reactivation. In circumstances where the orientation of the predefined faults and the cover base interface are poorly constrained we therefore advise caution regarding the interpretation of fault kinematics from systematic stepping fault segments.

Mandl (1987) has shown that faults contained in isotropic, homogeneous material will be discontinuous if continuous principal planes of stress cannot be defined (see also Treagus and Lisle, 1997). This result obviously raises the following question: What controls fault segmentation, non-plane stress fields or lithological/mechanical contrasts? The answer is probably both. Non-plane stress fields arise during lateral propagation of normal faults (screw dislocation; Cox and Scholz, 1988). However, they also develop if all principal axes of stress are oblique to interfaces of materials with contrasting mechanical properties (Treagus, 1981, 1988).

In both cases continuous principal surfaces of stress cannot be defined which will most likely result in the formation of discontinuous faults. It is not yet established whether the propagation process or mechanical stratigraphy is the dominant cause for fault segmentation, but we suggest that the scale of mechanical anisotropy plays a crucial role.

The synthetic fault zones developed in the experimental models with inclined base-cover interfaces are highly segmented and show the progressive formation of segments, relay ramps and segment linkage, where the degree of segmentation increases with increasing interface inclination. Since the models were conducted under well-defined boundary conditions there is no doubt that the individual segments are part of the same fault zone. Although a similar growth sequence is widely accepted for the growth of strike-slip faults (e.g. review by Sylvester, 1988) there is still an ongoing debate whether segmented normal fault zones are the result of linkage of initially isolated faults or whether the segments were always part of the same fault zone, i.e. the faults are kinematically coherent (Walsh et al., 2003). The experimental modelling results clearly favour the latter.

Our simple model provides geometrical predictions that are consistent with a natural fault zone within a limestone/shale sequence (Figs. 1 and 13). Stepping directions and, in particular, the degree of fault segmentation of normal faults are, however, likely to be also controlled by factors other than differences in the dip direction of fault and bedding. Although further research into the origin and nature of 3D changes in principal stress directions and discontinuous principal stress planes across interfaces within heterogeneous rock volumes is required, our experimental model, for which the boundary conditions were fully controlled, provides strong support for the importance of fault/bed geometrical configurations in the generation of segmented faults within multilayered sequences.

8 Conclusions

- A simple geometric model suggests that continuous normal faults exhibiting fault dip refraction in multilayers will also exhibit strike refraction if bedding is dipping and has a different strike to the fault zone. The amount of strike refraction is mainly a function of fault dip refraction and the orientation of bedding relative to the fault.
- The geometric model can be used to estimate the degree of fault segmentation, if it is assumed that faults nucleate first as dip-slip or extensional structures within the mechanically stronger lithology. Normal faults are expected to be segmented, if bedding is dipping and has a different strike to the fault zone, and the degree of segmentation is a function of bedding orientation, fault dip refraction and thickness ratio of the strong and weak layers comprising the multilayer.
- Our model of fault dip refraction and fault segmentation and/or strike refraction has been verified using a simple physical experiment which shows that fault refraction in dipping layers causes fault segmentation with predictable directions and degrees of stepping.
- Both experimental and geometrical evidence suggests that systematic stepping of normal faults in cover sequences above a predefined fault, such as a reactivated basement fault, is not necessarily an indicator of oblique-slip reactivation.

- Direct application of the model to natural fault zones is likely to be complicated by the operation of other factors that also control fault segmentation and/or strike refraction.

Acknowledgements

The sandbox experiments presented in this study were conducted in the Hans Ramberg Tectonic Laboratory. M. Schöpfer thanks the HRTL staff for their hospitality and assistance and is grateful to Sören Karlsson, master craftsman, for crafting the blocks for the experiments. Discussion with Sue Treagus is gratefully acknowledged. Constructive reviews by Dave Peacock, Roy Schlische and an anonymous reviewer and the editorial advice of Joao Hippertt are gratefully acknowledged. M. Schöpfer's PhD thesis project was funded by Enterprise Ireland (PhD Project Code SC/00/041) and a Research Demonstratorship at University College Dublin. This research was also partly funded by an Embark Postdoctoral Fellowship Scheme.

Appendix A

Derivation of Eq-1

The aim of this appendix is to derive an equation that can be used to construct the geometry of a continuous refracting fault in a periodically layered sequence. A list of symbols is provided in Table 1, Fig. A-1 shows both map view and cross-section of a continuous refracting fault within a periodically layered sequence, together with the stereonet solution (see Section 3.2). In order to construct this geometry we predefine the true dips of the fault within the two lithologies, θ_s and θ_w, and dip direction/dip of both bedding and average fault, ϕ_b/θ_b and ϕ_a/θ_a, respectively. The intersection of bedding with the average fault plane can then be used to determine the dip directions of the fault within the two lithologies, an exercise that can be easily done using a stereonet (see inset in Fig. A-1 and Figs. 2, 3 and 4). The thickness ratio of the two lithologies, t_s/t_w, cannot be obtained from the stereonet alone. However, an equation relating the orientations of fault and bedding to the thickness ratio can be easily derived in a cross section parallel to the dip direction of the average fault (Fig. A-1). If the strike of dipping bedding is not parallel to the average fault an apparent dip of bedding, θ'_b, will be observed on the fault normal cross section. As shown in this paper this orientation of bedding relative to the average fault will cause a change in strike of the fault within the strong and weak layers (strike refraction) and therefore apparent dips, θ'_s and θ'_w, are observed in cross section (Fig. A-1). The apparent dip, θ', of a plane in cross section can be obtained from the well-known relationship

$$\tan\theta' = \cos\delta\tan\theta, \tag{A-1}$$

where θ is the true dip and δ is the difference between the dip direction of the plane and the strike of the cross section. The three apparent dips observed in cross section are therefore given by:

$$\begin{aligned}\tan\theta'_b &= \cos(\phi_a - \phi_b)\tan\theta_b\\ \tan\theta'_s &= \cos(\phi_a - \phi_s)\tan\theta_s\\ \tan\theta'_w &= \cos(\phi_a - \phi_w)\tan\theta_w\end{aligned} \tag{A-2}$$

Also note that the layer thicknesses observed in cross section are apparent thicknesses if the bedding dip direction is not parallel to the strike of the cross section. The thicknesses observed in cross section are increased by a factor, which depends on the orientation of bedding relative to the cross section. Our aim, however, is to find an expression that relates the orientations of fault and bedding to the thickness ratio. Consequently a factor correcting for apparent thickness will cancel out.

The derivation of the desired equation is simplified by subtracting the apparent dip of bedding, θ'_b, from the fault dips (Fig. A-2):

$$\alpha = \theta'_s - \theta'_b \qquad \text{(A-3a)}$$

$$\beta = \theta'_w - \theta'_b \qquad \text{(A-3b)}$$

$$\gamma = \theta_a - \theta'_b \qquad \text{(A-3c)}$$

With the aid of the diagram shown in Fig. A-2 three equations can be obtained:

$$\tan\alpha = t_s / a \qquad \text{(A-4a)}$$

$$\tan\beta = t_w / b \qquad \text{(A-4b)}$$

$$\tan\gamma = (t_s + t_w)/(a+b) \qquad \text{(A-4c)}$$

Substitution of Eqs. (A-4a) and (A-4b) into (A-4c) and rearranging gives:

$$t_s\left(1 - \frac{\tan\gamma}{\tan\alpha}\right) = t_w\left(\frac{\tan\gamma}{\tan\beta} - 1\right) \qquad \text{(A-5)}$$

Finally, substitution of Eq. (A-3) into Eq. (A-5) and rearrangement gives the thickness ratio, t_s/t_w, as a function fault and bedding orientation (Eq. 1).

The dip directions of the fault in the strong and weak layers for a predefined thickness ratio can be obtained by systemically varying the average fault dip until the desired thickness ratio is obtained.

References

Childs, C., Watterson, J., Walsh, J.J., 1995. Fault overlap zones within developing normal fault systems. Journal of the Geological Society, London 152, 535-549.

Childs, C., Nicol, A., Walsh, J.J., Watterson, J., 1996. Growth of vertically segmented normal faults. Journal of Structural Geology 18, 1389-1397.

Cox, S.J.D., Scholz, C.H., 1988. On the formation and growth of faults: an experimental study. Journal of Structural Geology 10, 413-430.

Crider, J.G., Peacock, D.C.P., 2004. Initiation of brittle faults in the upper crust: a review of field observations. Journal of Structural Geology 26, 691-707.

Davison, I., 1987. Normal fault geometry related to sediment compaction and burial. Journal of Structural Geology 9, 393-401.

Dunham, K.C., 1948. Geology of the Northern Pennine Orefield. Volume 1. Tyne to Stainmore. Memoirs of the Geological Survey of Britain, London.

Dunham, K.C., 1988. Pennine mineralization in depth. Proceedings of the Yorkshire Geological Society 47, 1-12.

Ferrill, D.A., Morris, A.P., 2003. Dilational normal faults. Journal of Structural Geology 25, 183-196.

Glen, R.A., Hancock, P.L., Whittaker, A., 2005. Basin inversion by distributed deformation: the southern margin of the Bristol Channel Basin, England. Journal of Structural Geology 27, 2113–2134.

Goguel, J., 1982. Une interprétation méchanique de la réfraction de la schistosité. Tectonophysics 82, 125-143.

Horsfield, W.T., 1977. An experimental approach to basement-controlled faulting. Geologie en Mijnbouw 56, 363-370.

Hus, R., Acocella, V., Funiciello, R., De Batist, M., 2005. Sandbox models of relay ramp structure and evolution. Journal of Structural Geology 27, 459-473.

Imber, J., Tuckwell, G.W., Childs, C., Walsh, J.J., Manzocchi, T., Heath, A.E., Bonson, C.G., Strand, J., 2004. Three-dimensional distinct element modelling of relay growth and breaching along normal faults. Journal of Structural Geology 26, 1897-1911.

Jackson, P., 1987. The corrugation and bifurcation of fault surfaces by cross-slip. Journal of Structural Geology 9, 247-250.

Larsen, P.-H., 1988. Relay structures in Lower Permian basement-involved extension system, East Greenland. Journal of Structural Geology 10, 3-8.

Mandl, G., 1987. Discontinous fault zones. Journal of Structural Geology 9, 105-110.

Mandl, G., 1988. Mechanics of tectonic faulting. Models and Basic Concepts. Elsevier, Amsterdam.

Mandl, G., 2000. Faulting in brittle rocks. Springer, Berlin Heidelberg New-York.

Olson, J.E. 2004. Predicting fracture swarms - the influence of subcritical crack growth and the crack-tip process zone on joint spacing in rock. In: Cosgrove, J. W., Engelder, T., (Eds.), The initiation, propagation and arrest of joints and other fractures. Geological Society London Special Publication 231, 73-87.

Peacock, D.C.P., Sanderson, D.J., 1991. Displacements, segment linkage and relay ramps in normal fault zones. Journal of Structural Geology 13, 721-733.

Peacock, D.C.P., Sanderson, D.J., 1994. Geometry and development of relay ramps in normal fault systems. American Association of Petroleum Geoscientists Bulletin 78, 147-165.

Peacock, D.C.P., Zhang, X., 1993. Field examples and numerical modelling of oversteps and bends along normal faults in cross-section. Tectonophysics 234, 147-167.

Ramsay, J.G., Huber, M.I., 1987. The techniques of modern structural geology. Vol. 2: Folds and fractures. Academic Press Ltd, London.

Schöpfer, M.P.J., Childs, C., Walsh, J.J., 2006. Localisation of normal faults in multilayer sequences. Journal of Structural Geology 28, 816–833.

Segall, P., Pollard, D.D., 1980. Mechanics of discontinuous faults. Journal of Geophysical Research 85, 4337-4350.

Soliva, R., Benedicto, A., 2004. A linkage criterion for segmented normal faults. Journal of Structural Geology 26, 2251-2267.

Sibson, R.H., 1998. Brittle failure mode plots for compressional and extensional tectonic regimes. Journal of Structural Geology 20, 655-660.

Sibson, R.H., 2000. Fluid involvement in normal faulting. Journal of Geodynamics 29, 469-499.

Sylvester, A.G., 1988. Strike-slip faults. Geological Society of America Bulletin 100, 1666-1703.

Treagus, S.H., 1981. A theory of stress and strain variations in viscous layers, and its geological implications. Tectonophysics 72, 75-103.

Treagus, S.H., 1983. A theory of finite strain variation through contrasting layers, and its bearing on cleavage refraction. Journal of Structural Geology 5, 351-368.

Treagus, S.H., 1988. Strain refraction in layered systems. Journal of Structural Geology 10, 517-527.

Treagus, S.H., Lisle, R.J., 1997. Do principal surfaces of stress and strain always exist? Journal of Structural Geology 19, 997-1010.

Wallace, W., 1861. The laws which regulate the deposition of lead ores in veins: illustrated by an examination of the geological structure of the mining districts of Alston Moor, Stanford, London.

Walsh, J.J., Watterson, J., Bailey, W.R., Childs, C., 1999. Fault relays, bends and branch-lines. Journal of Structural Geology 21, 1019-1026.

Walsh, J.J., Bailey, W.R., Childs, C., Nicol, A., Bonson, C.G., 2003. Formation of segmented normal faults: a 3-D perspective. Journal of Structural Geology 25, 1251-1262.

Figure captions

Figure 1: Natural example of a refracted and segmented sinistral oblique-slip normal fault. (a) Map and cross-section of fault zone located NE of Quantock's Head (ST 13786 44559; see inset for location map), Kilve foreshore, Somerset, UK. Fault throw decreases from 40cm in the SE to 25cm in the NW. The fault is highly segmented both laterally (in map view) and vertically (viewed in cross-sections). White dot with arrow is slickenside lineation. Both the limestone and shale layers are laterally continuous with constant thickness; discontinuous layer map patterns are due to staircase-like erosion. Also note that the mapped area has significant topography, which generates an apparent right-stepping of the faults from one limestone bed to the other. The systematic stepping referred to in the text is observed within each limestone bed. The map was drawn at a scale of 1:100, whereas the cross-sections were constructed at a scale of 1:50; the sections are therefore slightly more detailed than the map. The cross-section shown is not a vertical slice through the fault zone, but a composite of three individual sections, which are highlighted in map as H-bars. (b) and (c): Photos of mapped fault zone. Standpoint and field of view of photos is shown on map. (b) Strike parallel photo of fault zone taken standing on layer III, with limestone layer II in the foreground and layer I in the background. Notice fault refraction. (c) Oblique photo of layer II showing a relay ramp that is developed between two right stepping fault segments within the limestone layer. FWF and HWF denote footwall and hangingwall fault, respectively. In all diagrams fault segment X is labelled for clarity.

Figure 2: Lower hemisphere, equal area stereoplots illustrating the problem of continuous refracting faults. Fault orientations are given as: (dip direction ϕ/dip θ). Bedding is oriented (180/30) and the average fault is oriented (270/60). The symbols and parameters used in this study are shown and summarized in Table 1. In (a) the intersection lineations of the fault in strong (l_s) and (l_w) weak layers and the average fault (l_a) with bedding are given and labelled in the stereonet. Since the intersection lines are not parallel to each other a continuous, refracting fault cannot exist: a continuous fault surface demands that the intersections with bedding are the same. In (b) the dip directions of the fault in the strong and weak layers were rotated in order to obtain a continuous refracting fault plane. Consequently the intersection lineations of the fault with bedding are parallel to each other.

Figure 3: Stereoplots and block diagrams illustrating the normal fault geometries discussed and analysed in this study. Bedding (180/45) and the average fault (270/59) orientation are the same in all diagrams and thickness ratio, t_s/t_w is 0.6. Measured parameters are shown in Fig. 2 and a list of symbols is given in Table 1. (a) Planar normal fault (i.e. with no dip or strike refraction) offsetting inclined bedding, for which the fault-bedding intersections for different layers are the parallel to each other. (b) Continuous refracting fault, a geometry that demands a difference in fault strike between different layers. The absolute strike change is greater in the less abundant layers (strong - stippled) than in the more abundant layers (weak - unornamented) and the change in dip direction is clockwise in the former and anticlockwise in the latter. (c) Block diagram of a segmented fault. For the sake of clarity segmentation is only shown for faults contained in the strong (stippled) layers. The en échelon segments have the same dip direction as the average fault. The dip of the segments is the

apparent dip (measured in a cross section normal the strike of the average fault) of a median plane passing through the en échelon arrays. The fault segments are layer-bound, right-stepping and pure dip-slip (slickensides are schematically indicated). The tip lines of individual segments are shown, for simplicity, as rectangular although in reality elliptical tip lines are perhaps more likely. If the fault contained in the weak layers were discontinuous rather than continuous the layer-bound dip-slip en échelon segments would be left-stepping.

Figure 4: Lower hemisphere, equal area stereoplots illustrating the problem of continuous refracting faults. Fault orientations are given as: (dip direction/dip). Bedding is oriented (180/30) and the average fault dip is 60º in all plots. In (a) a continuous fault plane does not exist, since the intersections of the fault planes and the bedding plane do not coincide. In (b) the strike of the shallow dipping fault is adjusted in order to form a continuous plane. This, however, leads to anti-clockwise rotation of the average fault plane. In (c) the strike of the steeply dipping fault is adjusted which results in a clockwise rotation of the average fault plane. Stereoplot in (d) illustrates a continuous refracting fault contained within a multilayer with a thickness ratio, t_s/t_w, of 1.4, which was calculated using Eq. (1).

Figure 5: Plot of dip of bedding versus difference in dip direction between average fault and bedding contoured for (a) strike refraction, ϕ_s - ϕ_w and (b) average fault dip, θ_a. Fault dips are 80° and 50° in the strong and weak layers, respectively, and the thickness ratio, t_s/t_w, is 1.0. All contour labels are in degrees.

Figure 6: (a) Maps and (b) cross sections of continuous refracting faults for various orientations of bedding. Fault dip in the strong (stippled) and weak layers (unornamented) is 80° and 50°, respectively, and the thickness ratio is 1.0. The average fault dips towards the west in all maps and the strike and dip symbol gives the orientation of bedding. The maps were drawn using the numerical results shown in Fig. 5.

Figure 7: Maps and graphs illustrating the impact of thickness ratio on the geometry of continuous refracting faults in periodically layered sequences. (a) Three map view examples for thickness ratios of 0.1, 1.0 and 10. Fault dip in the strong (stippled) and weak layers (unornamented) is 80° and 50°, respectively, the average fault dips towards the west and bedding dips 30°S. (b) and (c): Plots of differences in dip direction between the average fault and faults contained within the strong and weak layers, ϕ_s - ϕ_a and ϕ_w - ϕ_a, versus log thickness ratio, t_s/t_w, calculated for (a) five different ϕ_a - ϕ_b values and (b) selected dips within the strong and weak layers. In (b) the fault dips in the strong and weak layers are 80° and 50°, respectively, and the dip of bedding is 30°. In (c) the difference in dip direction between the average fault and bedding is 90° and the dip of bedding is 30°. The strike refraction in these diagrams is the vertical distance between corresponding labelled curves for the strong and weak layers. The intersections of the curves with the labelled vertical dashed lines (white dots) are the data used for constructing the maps shown in (a).

Figure 8: (a) Diagram illustrating the nomenclature used to describe en échelon arrays. (b) Illustration of the variation in fault array geometries for constant segment length, L, three different ψ-values and three different overlap to separation ratios. (c)

Illustration of the variation in fault array geometries similar to those shown in (b) for constant separation, *S*.

Figure 9: (a) Maps of en échelon fault arrays exposed at the top of the strong layers as a function of bedding orientation relative to the average fault. The average fault strikes N - S and dips towards the west. Thickness ratio, t_s/t_w, is 1.0. The overlap length to separation ratio is 3.0 and the size of the relays (i.e. rectangular overlap region) is held constant. Bold lines are traces of fault segments (tick towards hangingwall) and thin lines are structure contours of the bedding plane. The dip of median planes through the layer-bound fault arrays is 80°. Similar maps can be constructed for the weak layers. Note, however, that en échelon faults exposed on top of the weak layers would exhibit the opposite stepping. (b) Cross sections of the fault geometries shown in (a). Cross sections are drawn normal to the strike of the average fault and for each layer a section was randomly selected from the maps shown in (a). Since faults within a mechanical multilayer typically localise first within the strong layers as (Mode I) fractures, only faults within the strong layers are shown.

Figure 10: Diagrams illustrating the experimental set-ups for the three different sandbox models designed to test our geometrical approach. The models are shown at a finite throw of 2 cm and the sand cover is only partly shown (the surface of the deformed sand cover is schematically shown as dashed line). The dip of the base-cover interface is 0, 10 and 20° in (a), (b) and (c), respectively. The sand cover in (a) had a uniform thickness of 6.1 cm. The sand covers in (b) and (c) were wedge shaped, 7.7 cm thick in the west and 2.5 cm thick in the east in (b), and 12.2 cm thick in the west and 1.3 cm thick in the east in (c). See text for further explanation.

Figure 11: Stereonet predictions of fault orientations in the sand cover (using a fault dip of 61.5°), map views of models at a predefined fault throw of 6 mm, and cross sections at a finite throw of 20 mm for the three different experiments (see Fig. 10 for boundary conditions). Only the centre of each model is shown in map view and ticks in the map views indicate locations of cross sections.

Figure 12: Photographs of the top surface of sand cover above 20° dipping base-cover interface (see Figs. 10c and 11c). The throw (*t*) of the predefined fault at the different stages of model evolution is shown. The dash-dot line at a predefined fault throw of 0 mm is the intersection between the predefined fault (dipping 45°S) and the base-cover interface (dipping 20°W); the solid lines are the predicted traces of the syn- and antithetic fault with ticks towards secondary graben. The predictions of fault orientations are also shown at a finite predefined fault throw of 20 mm, together with the footwall and hangingwall cut-offs of the predefined fault (dash-dot lines). The secondary graben diverges towards the west, where the cover is thicker.

Figure 13: Lower hemisphere, equal area stereoplots of orientation data of mapped fault zone shown in Fig. 1. In (a) the raw data are shown, together with great circles of the mean orientations, and a slickenside lineation within the shale. In (b) the average orientations and the lineation are rotated in such a way that the fault within the shale is dipping 50° and pure dip-slip and bedding is dipping towards the south (these rotations permit easy comparison with the model geometries of Figs. 3 and 4). Notice that our geometrical model would predict fault segmentation, with right-stepping segments (see relay ramp in Fig. 1c).

Figure A-1: Geometry of a continuous refracting fault in periodically layered sequence as seen in map view and cross section. The true dip of the fault in the strong (stippled) and weak (unornamented) layers is 80º and 50º, respectively. Thickness ratio, t_s/t_w, is 2/3 and the difference in dip direction between the average fault (270/57) and bedding (210/40) is 60º. Styles of poles and great circles in stereonet are the same as in Fig. 2 and 4. Parameters used throughout the paper are labelled.

Figure A-2: Diagram showing a selection of angular relationships and parameters used in the derivation of Eq. (1). See Appendix A for further explanation.

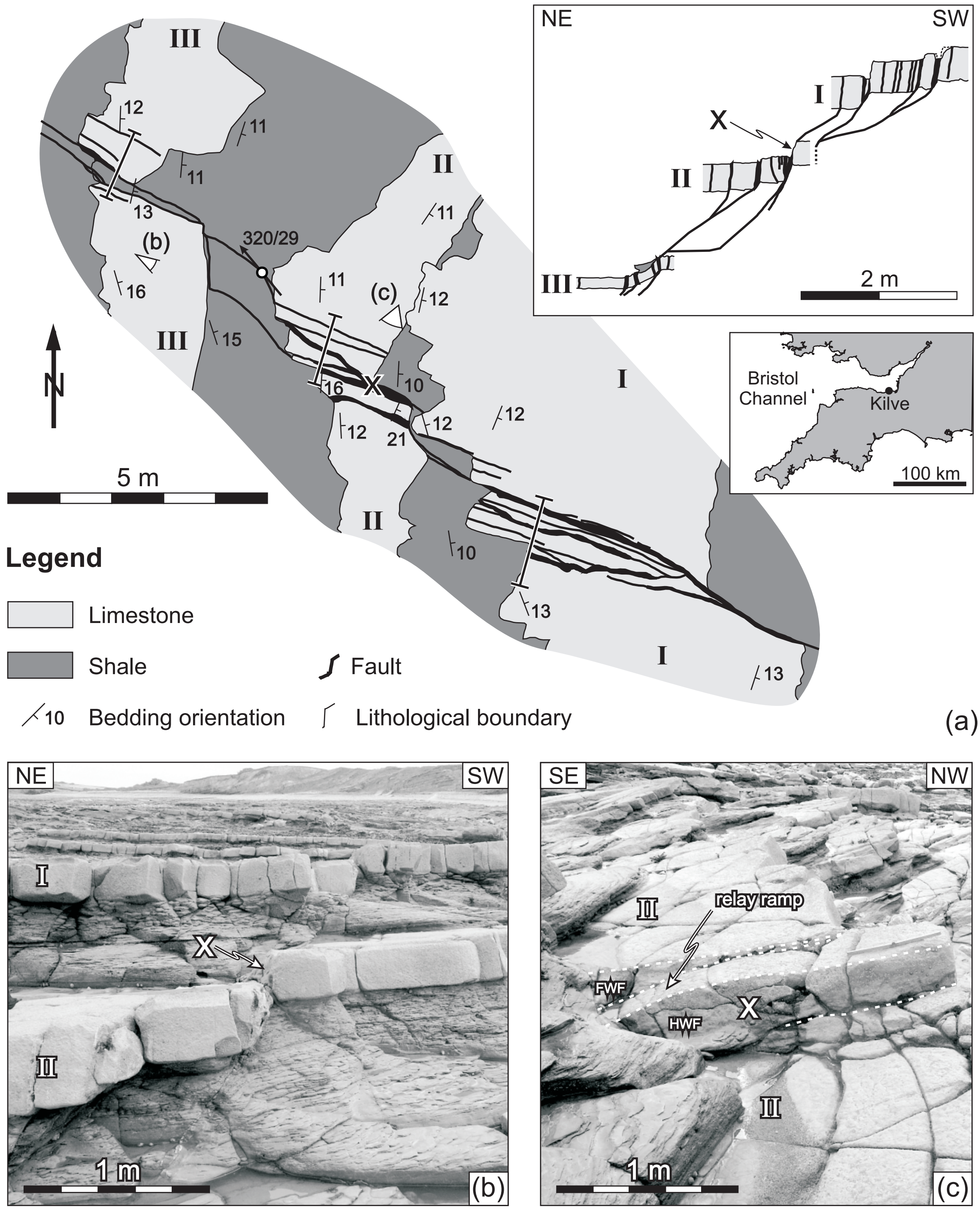

NE
SW
I
X
II
III
2 m
Bristol Channel
Kilve
100 km
III
12
11
11
13
(b)
16
III
15
320/29
II
11
11
(c)
12
16
X
10
12
12
12
21
I
5 m
II
10
13
I
13
Legend
Limestone
Shale
Fault
10 Bedding orientation
Lithological boundary
(a)
NE
SW
I
X
II
1 m
(b)
SE
NW
II
relay ramp
FWF
HWF
X
II
1 m
(c)

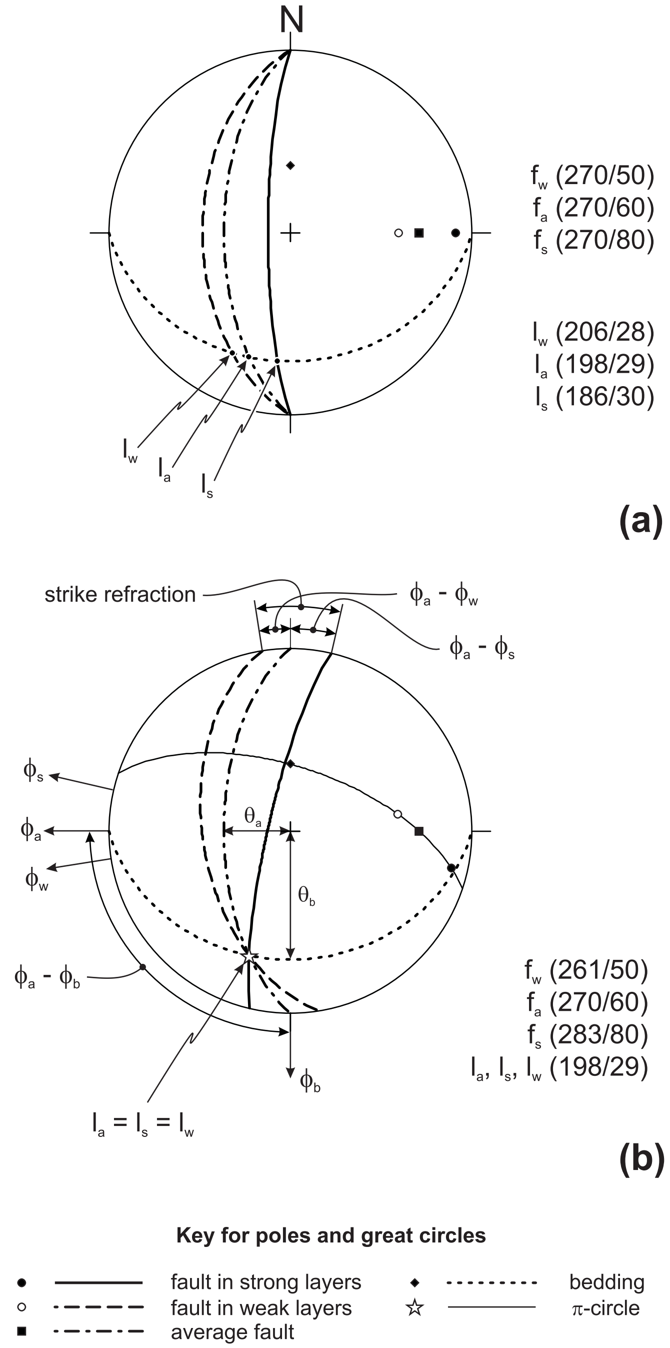

N
f_w (270/50)
f_a (270/60)
f_s (270/80)
l_w (206/28)
l_a (198/29)
l_s (186/30)
l_w
l_a
l_s
(a)
strike refraction
ϕ_a - ϕ_w
ϕ_a - ϕ_s
ϕ_s
ϕ_a
ϕ_w
θ_a
θ_b
ϕ_a - ϕ_b
ϕ_b
f_w (261/50)
f_a (270/60)
f_s (283/80)
l_a, l_s, l_w (198/29)
l_a = l_s = l_w
(b)
Key for poles and great circles
fault in strong layers
fault in weak layers
average fault
bedding
π-circle

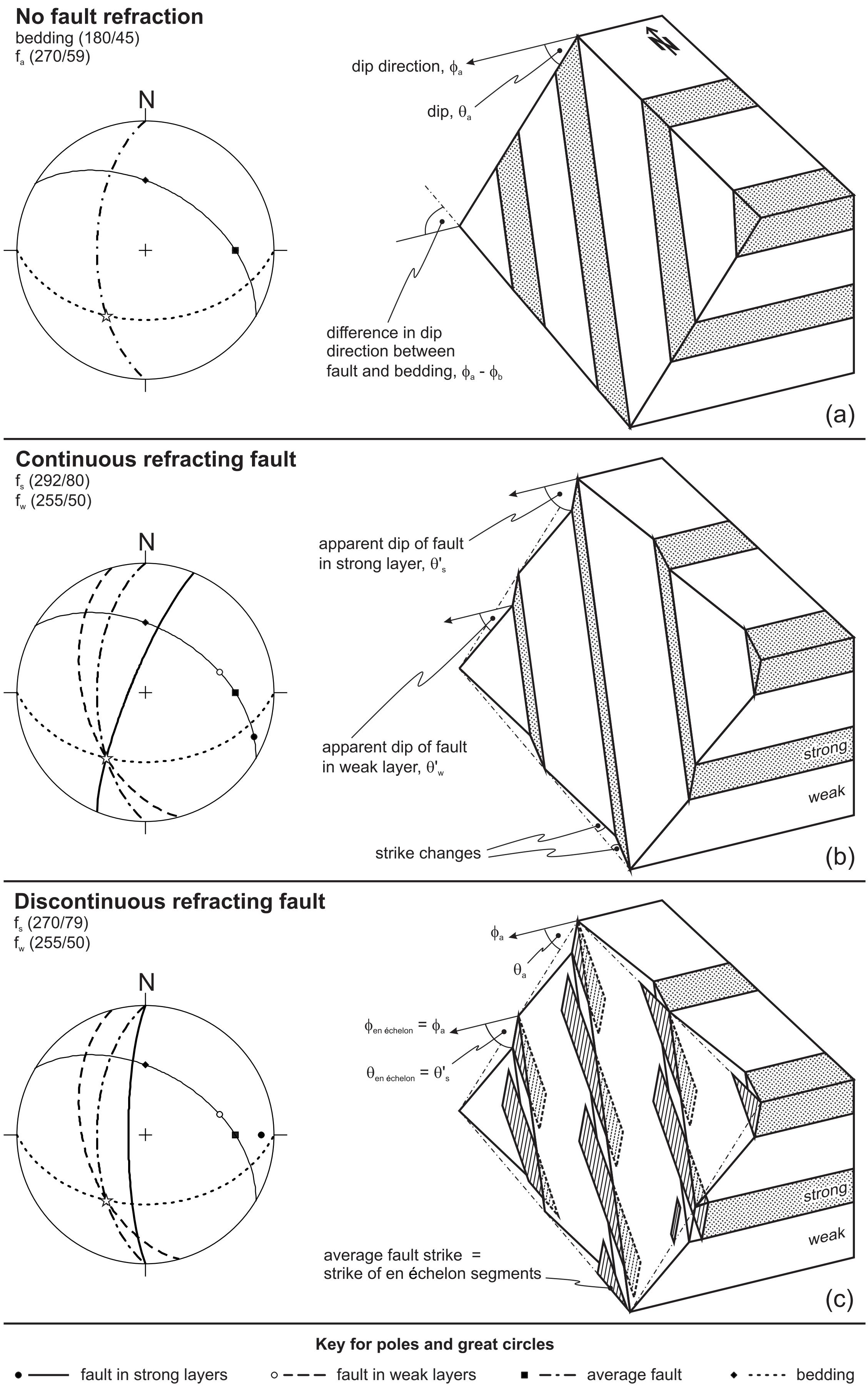
No fault refraction
bedding (180/45)
f_a (270/59)
N
dip direction, ϕ_a
dip, θ_a
difference in dip direction between fault and bedding, ϕ_a - ϕ_b
(a)
Continuous refracting fault
f_s (292/80)
f_w (255/50)
N
apparent dip of fault in strong layer, θ'_s
apparent dip of fault in weak layer, θ'_w
strike changes
strong
weak
(b)
Discontinuous refracting fault
f_s (270/79)
f_w (255/50)
N
ϕ_a
θ_a
$\phi_{en\ échelon} = \phi_a$
$\theta_{en\ échelon} = \theta'_s$
average fault strike = strike of en échelon segments
strong
weak
(c)
Key for poles and great circles
fault in strong layers
fault in weak layers
average fault
bedding

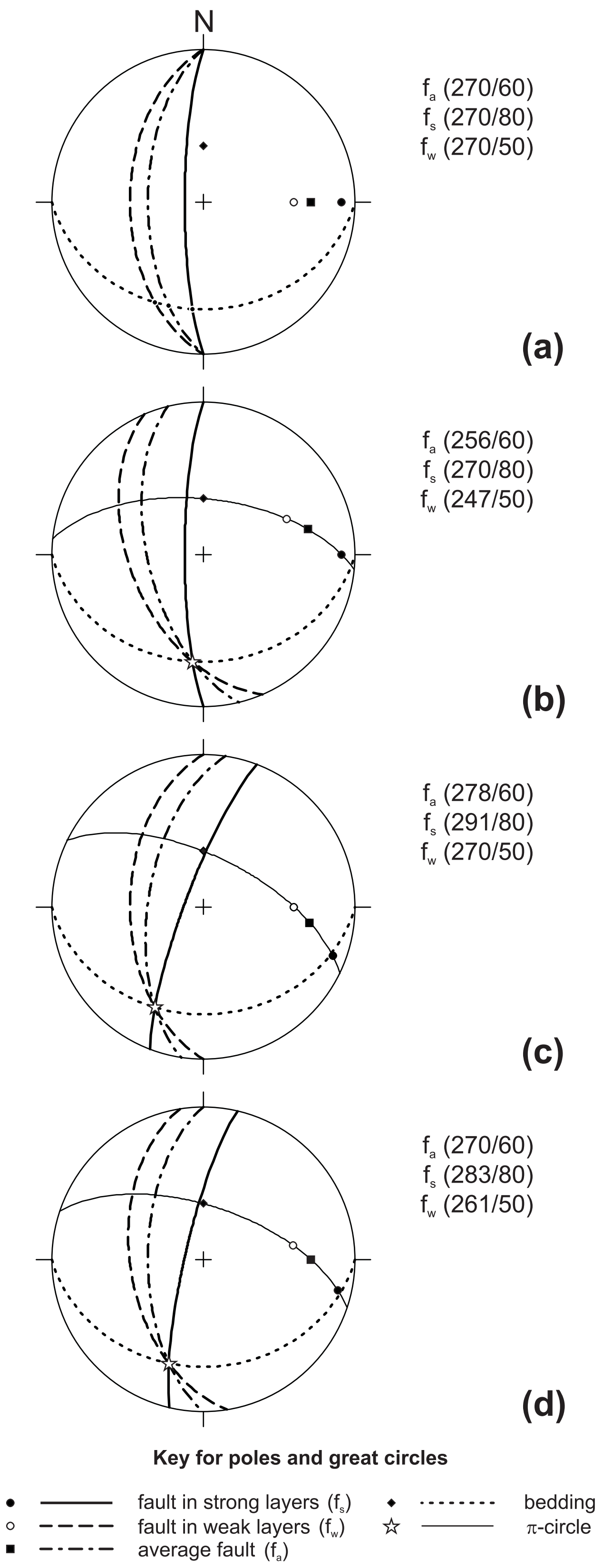
N
f_a (270/60)
f_s (270/80)
f_w (270/50)
(a)
f_a (256/60)
f_s (270/80)
f_w (247/50)
(b)
f_a (278/60)
f_s (291/80)
f_w (270/50)
(c)
f_a (270/60)
f_s (283/80)
f_w (261/50)
(d)
Key for poles and great circles
fault in strong layers (f_s)
fault in weak layers (f_w)
average fault (f_a)
bedding
π-circle

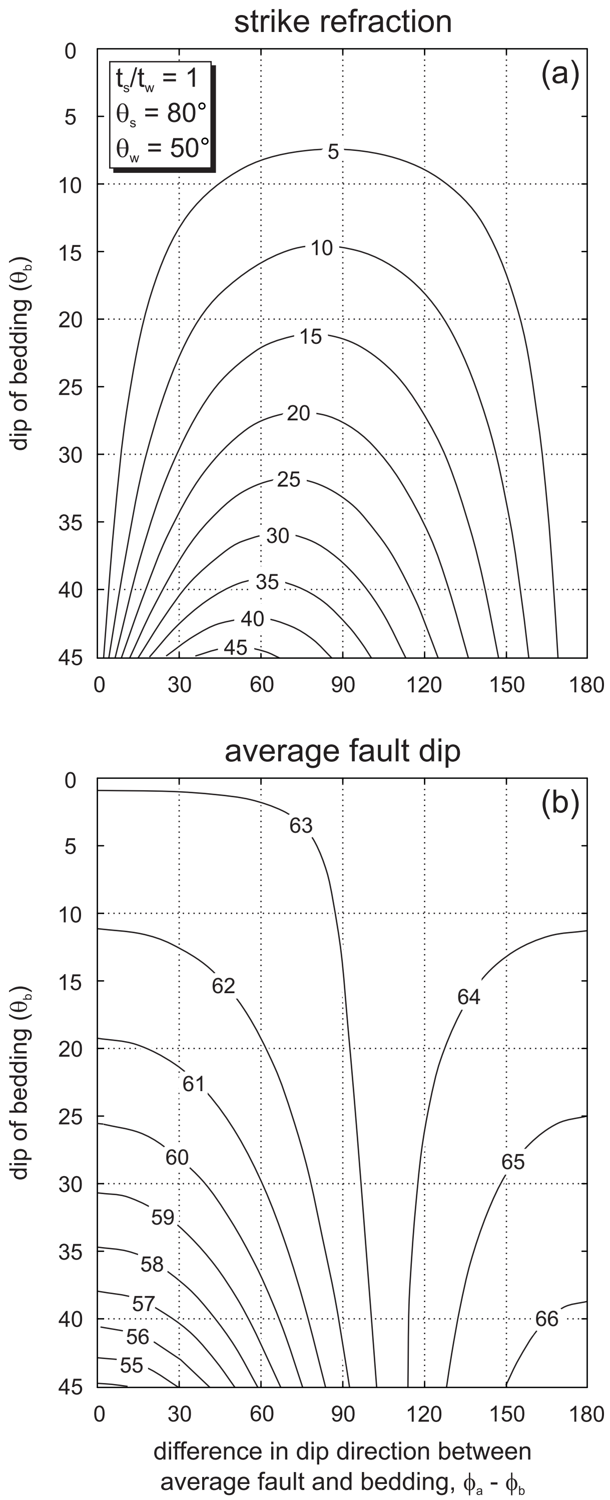

strike refraction
(a)
$t_s/t_w = 1$
$\theta_s = 80°$
$\theta_w = 50°$
5
10
15
20
25
30
35
40
45
dip of bedding (θ_b)
average fault dip
(b)
63
62
61
60
59
58
57
56
55
64
65
66
0
30
60
90
120
150
180
difference in dip direction between average fault and bedding, $\phi_a - \phi_b$

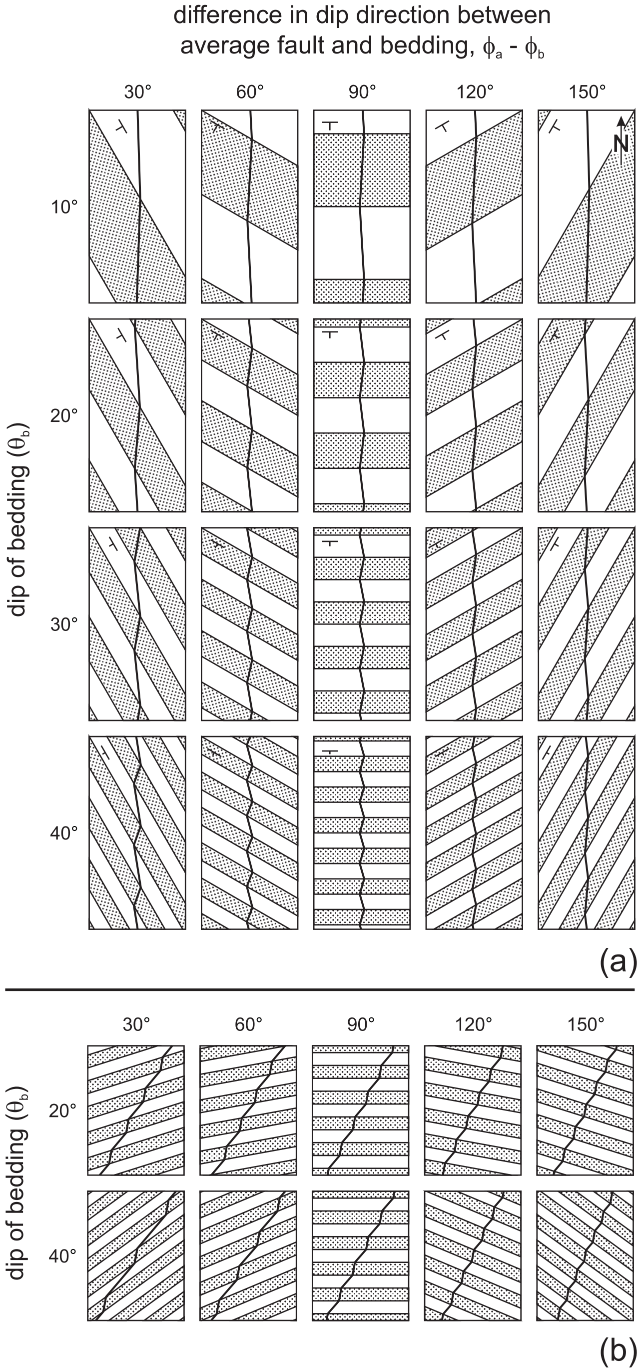
difference in dip direction between
average fault and bedding, $\phi_a - \phi_b$
30°
60°
90°
120°
150°
N
10°
20°
30°
40°
dip of bedding (θ_b)
(a)
30°
60°
90°
120°
150°
20°
40°
dip of bedding (θ_b)
(b)

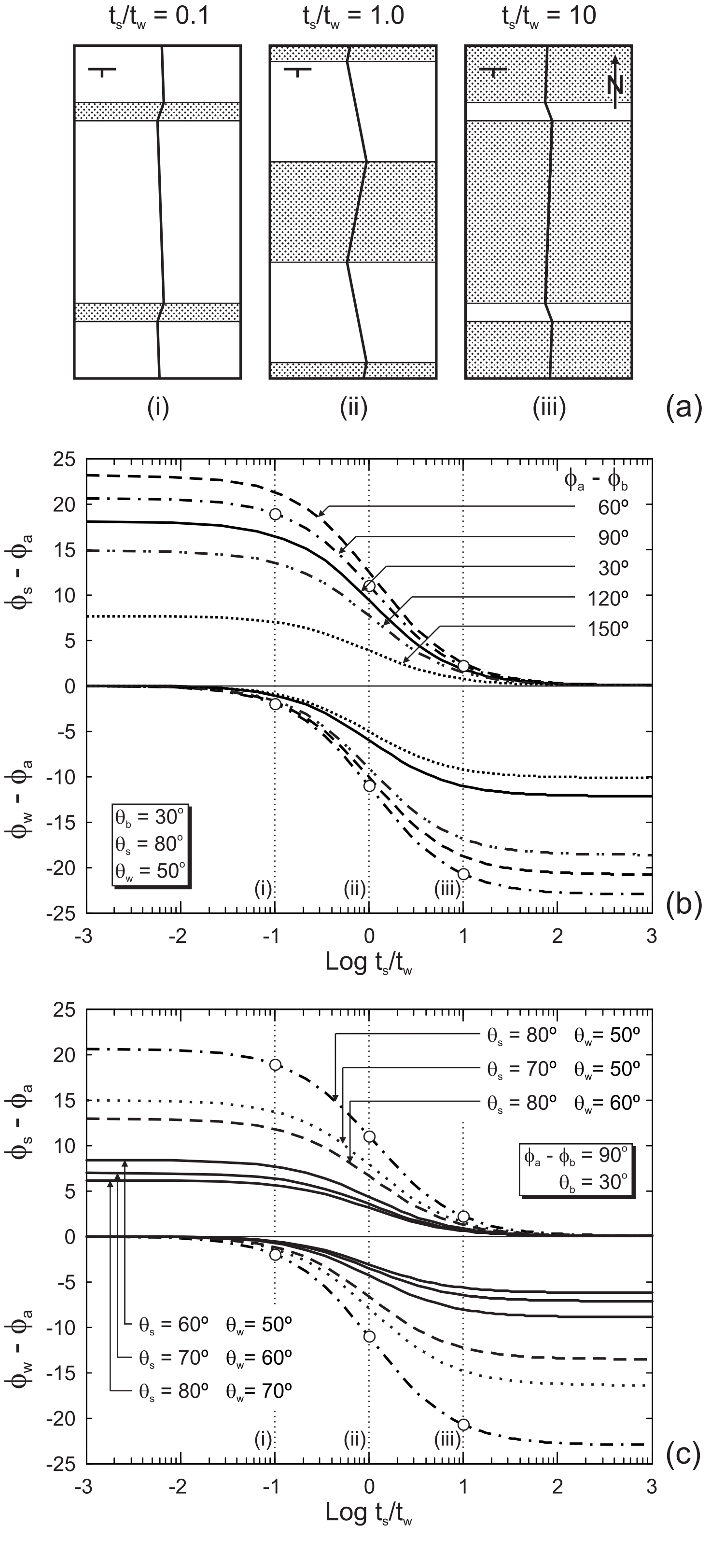

ts/tw = 0.1
ts/tw = 1.0
ts/tw = 10
(i)
(ii)
(iii)
(a)
φa - φb
60º
90º
30º
120º
150º
φs - φa
φw - φa
θb = 30°
θs = 80°
θw = 50°
(b)
Log ts/tw
θs = 80º θw= 50º
θs = 70º θw= 50º
θs = 80º θw= 60º
φa - φb = 90°
θb = 30°
θs = 60º θw= 50º
θs = 70º θw= 60º
θs = 80º θw= 70º
(c)

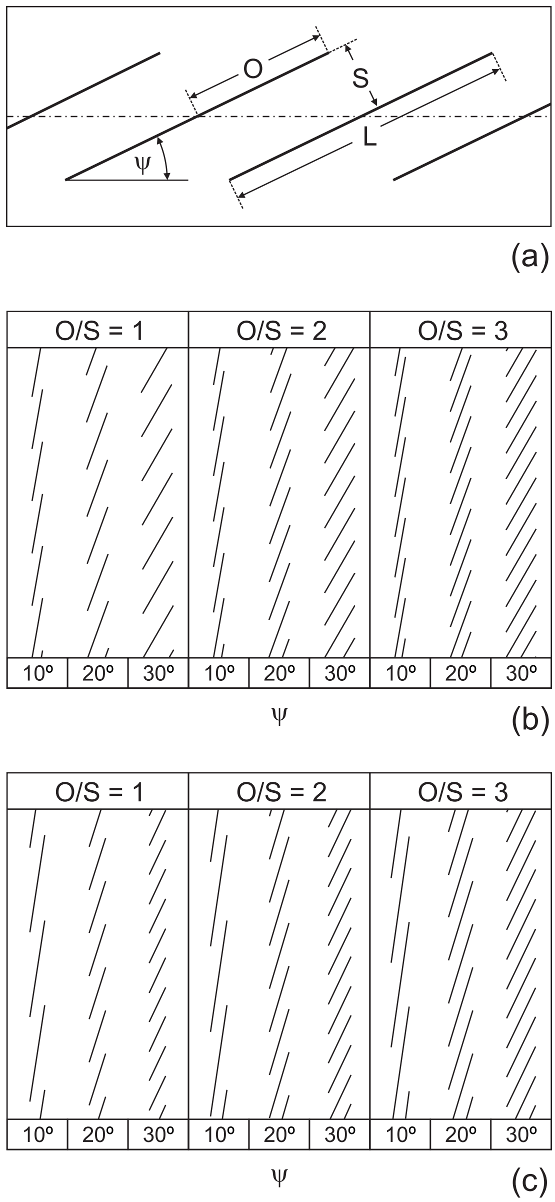
O
S
L
ψ
(a)
O/S = 1
O/S = 2
O/S = 3
10º
20º
30º
ψ
(b)
O/S = 1
O/S = 2
O/S = 3
10º
20º
30º
ψ
(c)

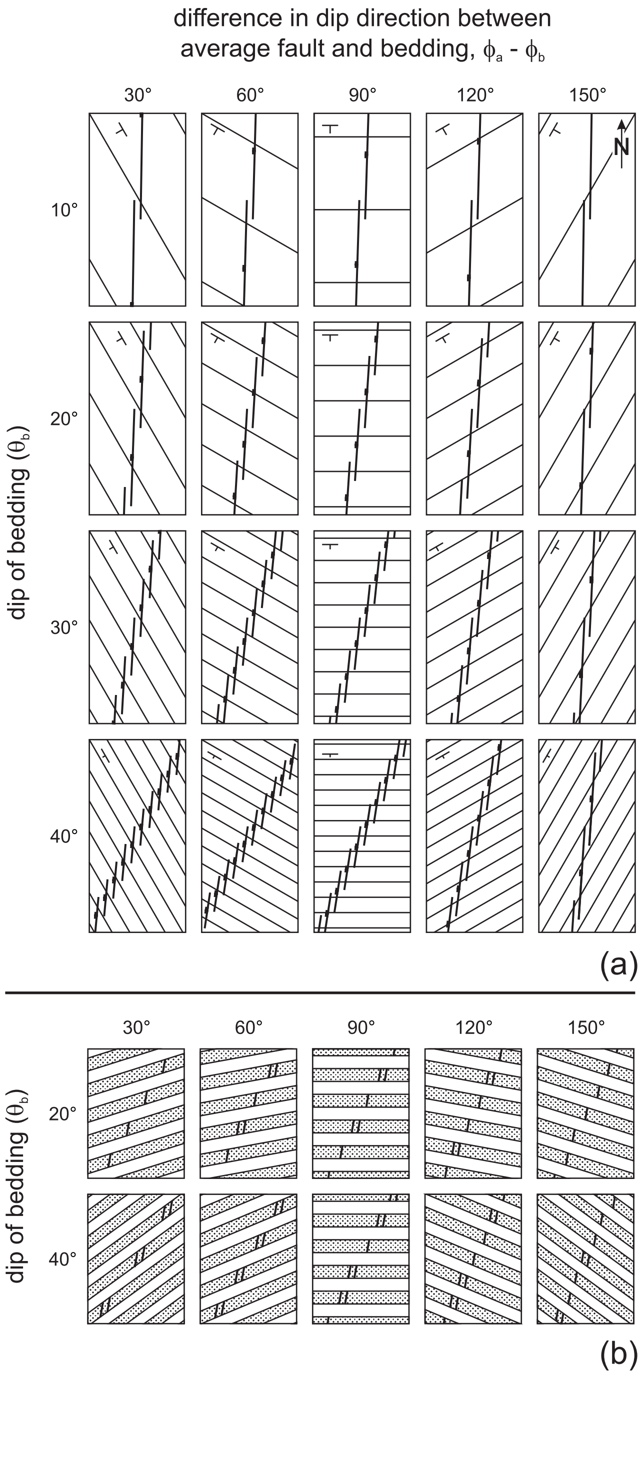
difference in dip direction between
average fault and bedding, ϕ_a - ϕ_b
30°
60°
90°
120°
150°
N
dip of bedding (θ_b)
10°
20°
30°
40°
(a)
30°
60°
90°
120°
150°
dip of bedding (θ_b)
20°
40°
(b)

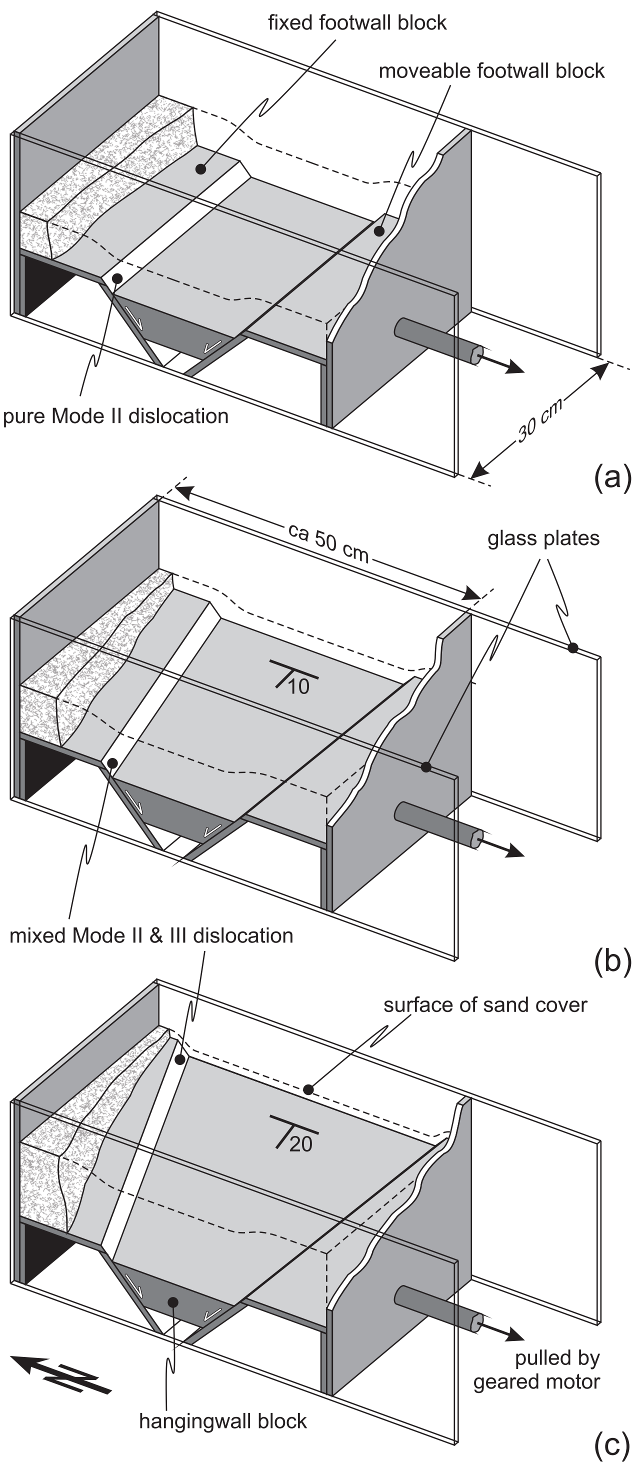
fixed footwall block
moveable footwall block
pure Mode II dislocation
30 cm
(a)
ca 50 cm
glass plates
$\overline{/}_{10}$
mixed Mode II & III dislocation
(b)
surface of sand cover
$\overline{/}_{20}$
pulled by geared motor
hangingwall block
(c)

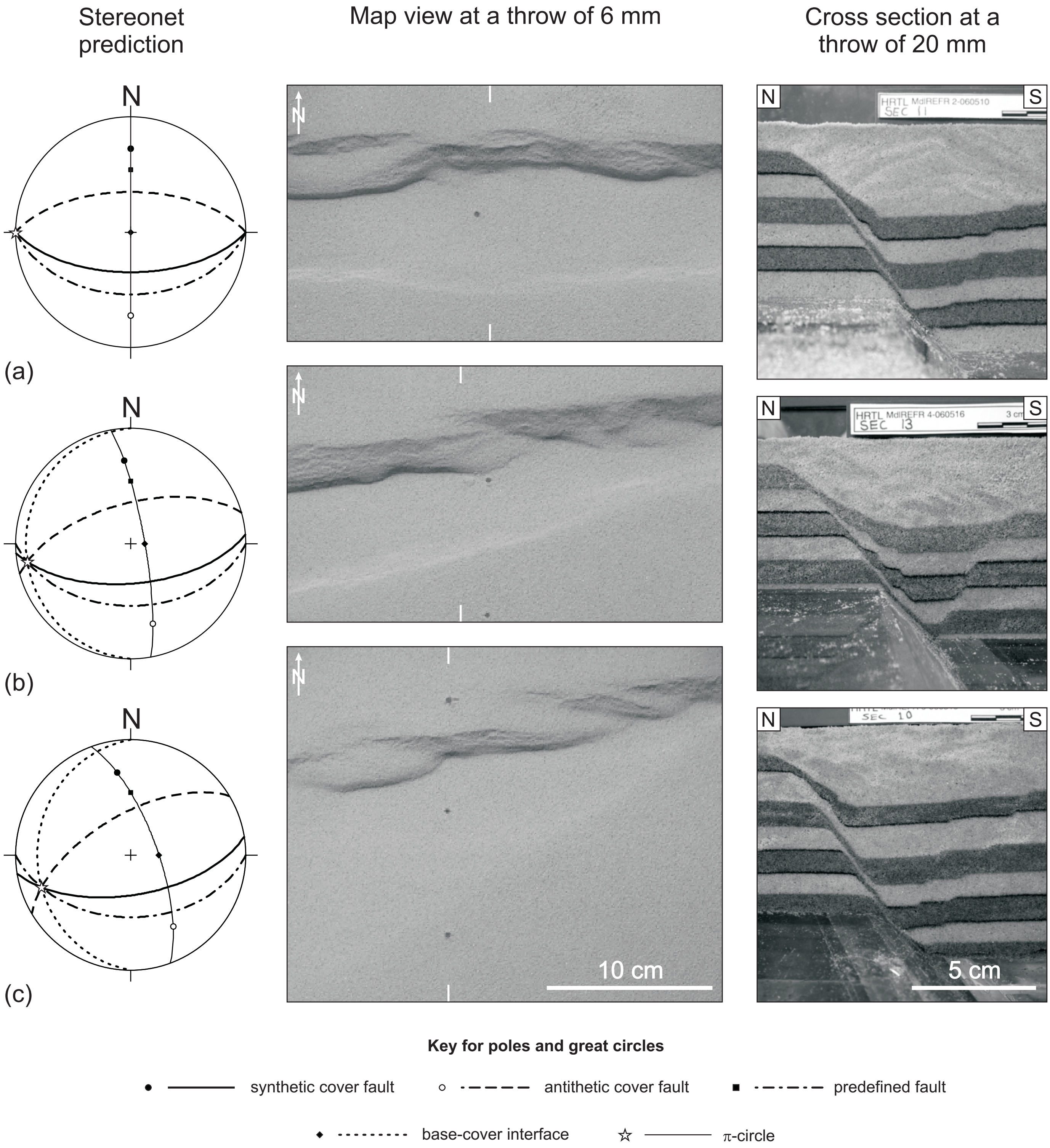

Stereonet prediction
Map view at a throw of 6 mm
Cross section at a throw of 20 mm
N
(a)
(b)
(c)
S
HRTL MdlREFR 2-060510
SEC 11
HRTL MdlREFR 4-060516
SEC 13
3 cm
SEC 10
10 cm
5 cm
Key for poles and great circles
synthetic cover fault
antithetic cover fault
predefined fault
base-cover interface
π-circle

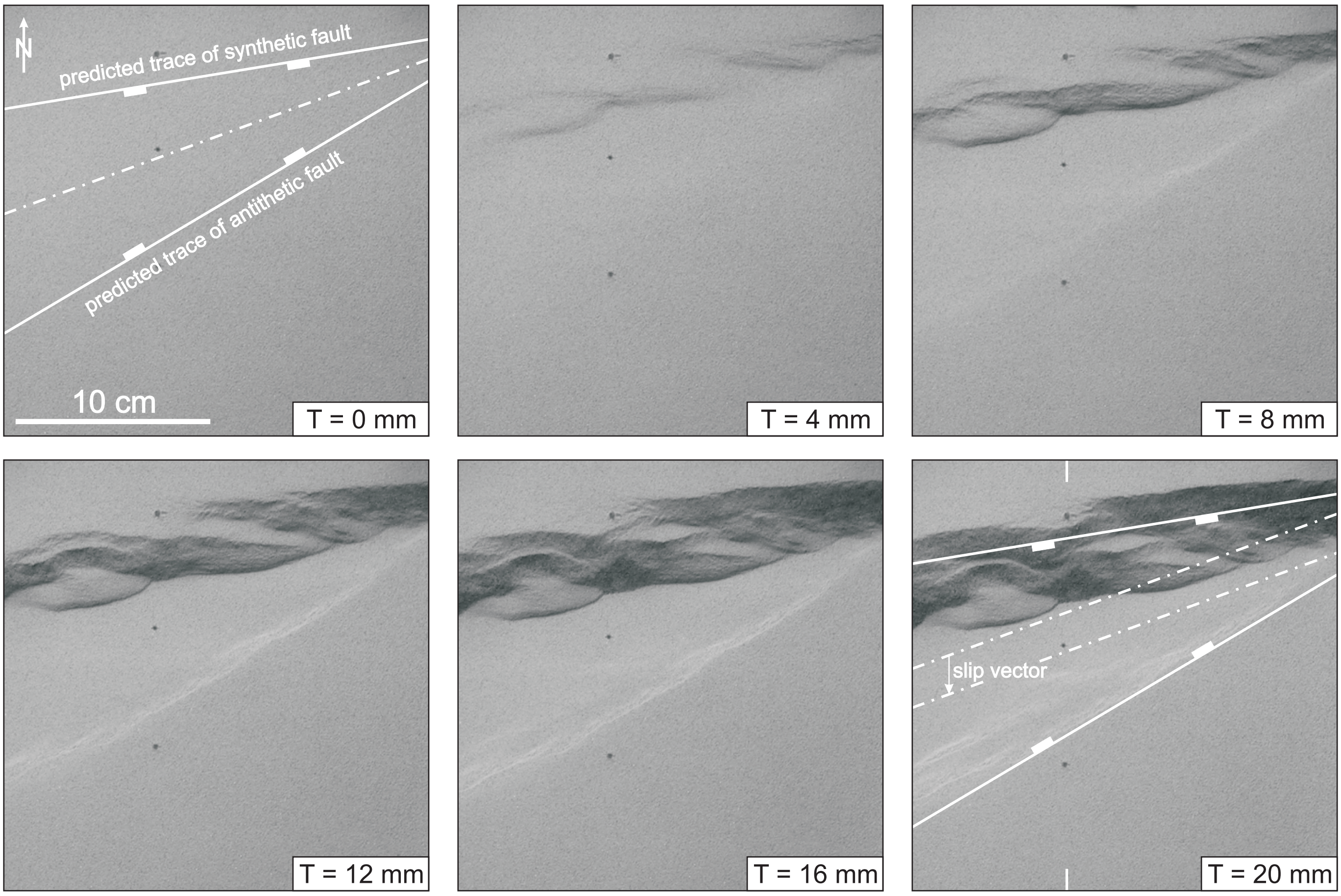

N
predicted trace of synthetic fault
predicted trace of antithetic fault
10 cm
T = 0 mm
T = 4 mm
T = 8 mm
T = 12 mm
T = 16 mm
slip vector
T = 20 mm

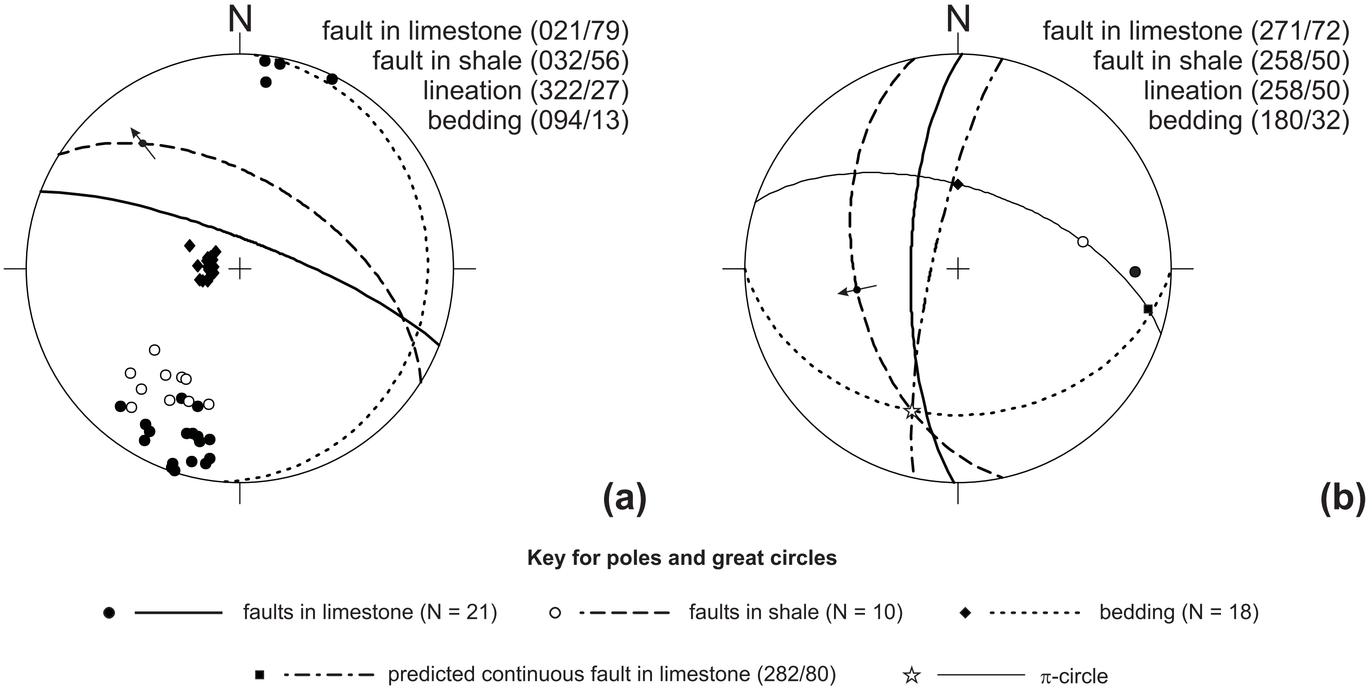
N
fault in limestone (021/79)
fault in shale (032/56)
lineation (322/27)
bedding (094/13)
(a)
N
fault in limestone (271/72)
fault in shale (258/50)
lineation (258/50)
bedding (180/32)
(b)
Key for poles and great circles
faults in limestone (N = 21)
faults in shale (N = 10)
bedding (N = 18)
predicted continuous fault in limestone (282/80)
π-circle

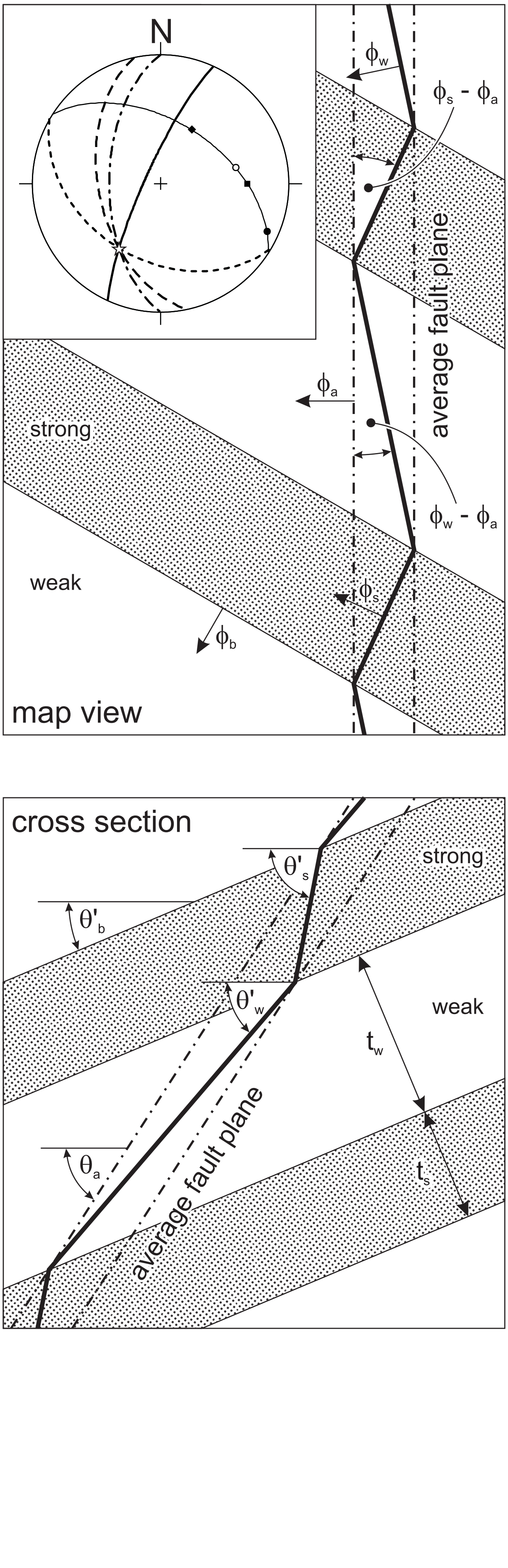

N
ϕ_w
ϕ_s - ϕ_a
average fault plane
ϕ_a
strong
ϕ_w - ϕ_a
weak
ϕ_s
ϕ_b
map view
cross section
θ'_s
strong
θ'_b
θ'_w
weak
t_w
θ_a
average fault plane
t_s

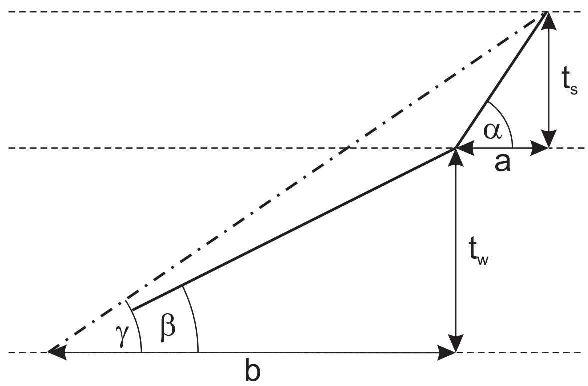

t_s
α
a
t_w
γ
β
b